1. Introduction

Discrete approximation of pressure gradient force in topography-following coordinates has been a long standing problem in atmospheric and ocean modeling (Gary, 1973; Mesinger & Arakawa, 1976; Janjic, 1977; Mesinger, 1982; Arakawa & Suarez, 1983; Mesinger & Janjic, 1985; Michailovich & Janjic, 1986; Blumberg & Mellor, 1987; Haney, 1991; Mellor *et al*, 1994; Song & Haidvogel, 1994; Lin, 1997; Janjic, T., 1998; Mellor *et al*, 1998; Song, 1998; Song & Wright, 1998).

The main difficulty is associated with so-called hydrostatic inconsistency, i.e., failure of the discretized pressure gradient force to vanish in the case when isopycnals are horizontal. This effect causes spurious geostrophically balanced flows, which in ocean models may often be as large as 10 cm/sec or more, degrading the quality of numerical solution beyond an acceptable limit. The problem is due to deviation of quasi-horizontal coordinates from either geopotential or isopycnic surfaces, so that the pressure gradient force in the r.h.s. of the momentum equations appears in form of two large terms which tend to cancel each other,

$$-\frac{1}{\rho_0}\frac{\partial P}{\partial x}\bigg|_z = -\frac{1}{\rho_0}\frac{\partial P}{\partial x}\bigg|_s + \frac{1}{\rho_0}\cdot\frac{\partial P}{\partial z}\cdot\frac{\partial z}{\partial x}\bigg|_s\,, \qquad (1.1)$$

where P is pressure; $\rho_0 =$ const is the usual mean density in a Boussinesq approximation; z is vertical coordinate in non-transformed (i.e., physical) space. Subscript z in $\partial/\partial x|_z$ means that the associated partial derivative is computed with respect to a constant geopotential surface, $z =$ const; while similar subscript s means that the differentiation is performed along the model coordinate surface, $s =$ const.

In the present study we avoid using the notion of σ-coordinate,

$$z(x,y,\sigma) = h(x,y)\cdot f(\sigma)\,, \qquad -1\le\sigma\le 0\,, \qquad (1.2)$$

where $h(x,y)$ is depth of bottom, and $f(\sigma)$ is a mapping function (independent of horizontal coordinates) which controls stretching of vertical coordinate. Instead it is assumed that the three-dimensional mapping function $z = Z(x,y,s)$ is *nonseparable*, and, generally speaking,

$$\frac{\partial Z}{\partial x}\bigg|_s \neq 0\,. \qquad (1.3)$$

Moreover, it is assumed that (1.1) may be *stiff* in the sense that

$$\epsilon \equiv \frac{\left|\frac{\partial P}{\partial x}\big|_s - \frac{\partial P}{\partial z}\cdot\frac{\partial z}{\partial x}\big|_s\right|}{\left|\frac{\partial P}{\partial x}\big|_s\right| + \left|\frac{\partial P}{\partial z}\cdot\frac{\partial z}{\partial x}\big|_s\right|} \ll 1\,, \qquad (1.4)$$

which indicates that a special precaution needs to be taken to avoid loss of accuracy.

The pressure P is computed from the hydrostatic equation,

$$P(x,y,z) = g\int_z^{\zeta}\rho(x,y,z')\mathrm{d}z'\,, \qquad (1.5)$$

where $\rho(x,y,z)$ is density, ζ is free surface elevation, and g is acceleration of gravity. One might be tempted to replace (1.1) with

$$-\frac{1}{\rho_0}\frac{\partial P}{\partial x}\bigg|_z = -\frac{1}{\rho_0}\frac{\partial P}{\partial x}\bigg|_s - \frac{g\rho}{\rho_0}\cdot\frac{\partial z}{\partial x}\bigg|_s\,, \qquad (1.6)$$

and discretize it in a straightforward way using standard second-order averaging and differencing operators. This was shown to be prone to hydrostatic consistency error (cf., Mesinger & Arakawa, 1976), caused mainly by the vertical averaging of pressure and horizontal averaging of density in (1.6) in order to co-locate them with horizontal velocity components on a staggered grid.

Practical experience has resulted in essentially two approaches to overcome this problem:

(*i*) In each vertical column compute a set of values of pressure, $P_k+\frac{1}{2}$, naturally located half-way between the density points on staggered vertical grid; then for each two neighboring columns, interpolate this pressure field to an appropriate common geopotential level; and then subtract the interpolated values. Note, that after computation of pressure, the density field ρ_k does not participate in any further computation. Obviously, in this approach the two terms in (1.1) become inseparable. The different methods of this family may be vary in details of choice of the common level as well as interpolation technique, which is mostly linear (Janjic, 1977; Arakawa & Suarez, 1983) or parabolic (Michailovich & Janjic, 1986). Overall, the overwhelming majority of atmospheric models use techniques which belong to this class.

(*ii*) Following Blumberg & Mellor, 1987 and Song, 1998, Eqs. (1.1)—(1.5) are first transformed into

$$-\frac{1}{\rho_0}\frac{\partial P}{\partial x}\bigg|_z = -\frac{1}{\rho_0}\frac{\partial P}{\partial x}\bigg|_{z=\zeta} - \frac{g}{\rho_0}\int_z^{\zeta}\frac{\partial\rho}{\partial x}\bigg|_z\mathrm{d}z' = \qquad (1.7)$$

$$= -\frac{g\rho(\zeta)}{\rho_0}\frac{\partial\zeta}{\partial x} - \frac{g}{\rho_0}\int_z^{\zeta}\left[\frac{\partial\rho}{\partial x}\bigg|_s - \frac{\partial\rho}{\partial z'}\frac{\partial z'}{\partial x}\bigg|_s\right]\mathrm{d}z'\,,$$

where, the expression in square brackets is similar to (1.1), except that P is replaced with ρ. Eq. (1.7) is then

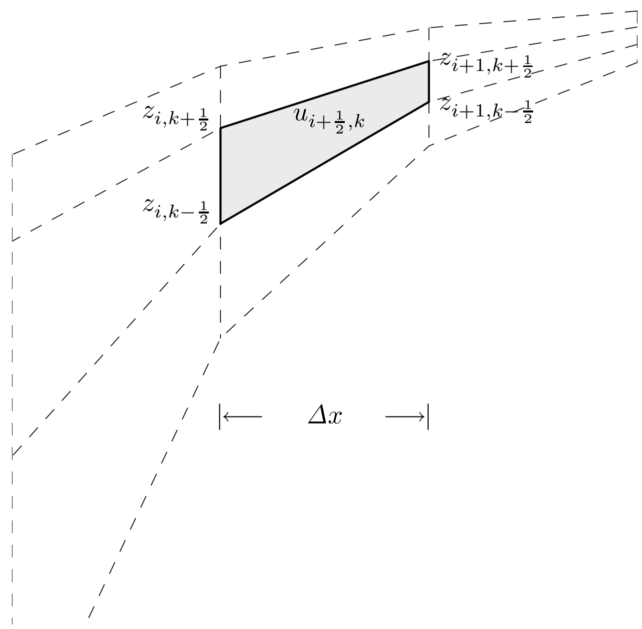

Figure 1. A fragment of x-z cross-section of the model grid. The shaded trapezoidal element repesents the $u_{i+\frac{1}{2},k}$.

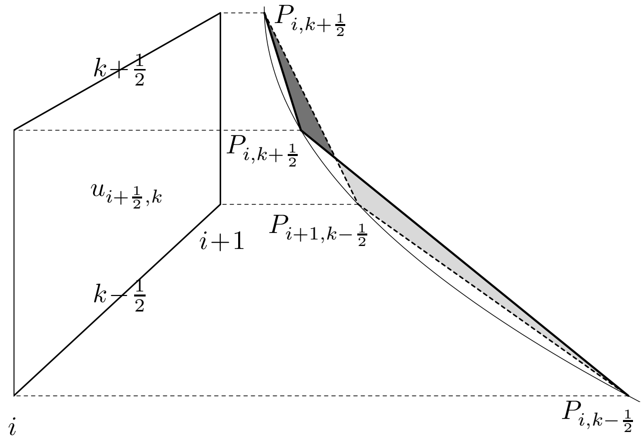

Figure 2. Explanation of hydrostatic error in Lin's method.

static consistency error in the case when density is a quadratic function of depth. The methodology we employ is based on the reconstruction of the density field as a *continuous* function of two coordinates (vertical and one horizontal) with subsequent analytic integration to compute a pressure field which is *exactly* and in a *continuous* sense hydrostatically consistent with the reconstructed density. The pressure field is then integrated analytically along the contour surrounding the velocity cell to compute the net pressure gradient force in a finite-volume sense.

2. Lin's Method

Lin, 1997 proposed to compute the horizontal pressure gradient force applied to a control-volume element around velocity component point $u_{i+\frac{1}{2},k}$ (see Fig. 1) by integrating pressure along the surface of that element (cf., Eq. (3) in Lin, 1997),

$$PGF_{i+\frac{1}{2},k} = \oint P(x',z')(\mathbf{n}\cdot\mathbf{1_x})\mathrm{d}l\,, \tag{2.1}$$

where the contour integral is taken in clockwise direction, $\mathbf{n}$ is the unit vector normal to the contour line and pointing inward, and $\mathbf{1_x}$ is the unit vector in the positive horizontal (geopotential) direction.

For the trapezoidal element in Fig. 1 , (2.1) becomes

$$PGF_{i+\frac{1}{2},k} = \int\limits_{x,z_{i,k-\frac{1}{2}}}^{x,z_{i,k+\frac{1}{2}}} P\,\mathrm{d}z' - \int\limits_{x,z_{i+1,k-\frac{1}{2}}}^{x,z_{i+1,k+\frac{1}{2}}} P\,\mathrm{d}z' + \tag{2.2}$$
$$+ \int\limits_{x,z_{i,k+\frac{1}{2}}}^{x,z_{i+1,k+\frac{1}{2}}} P\,\frac{\partial z}{\partial x}\bigg|_{s=\mathrm{const}} dx' - \int\limits_{x,z_{i,k-\frac{1}{2}}}^{x,z_{i+1,k-\frac{1}{2}}} P\,\frac{\partial z}{\partial x}\bigg|_{s=\mathrm{const}} \mathrm{d}x'\,,$$

where all four integral are understood as line integrals. The coordinate x' runs along the upper and lower facets of the grid element which have the slopes $\frac{\partial z}{\partial x}\big|_{s=\mathrm{const}} = \left(z_{i+1,k\pm\frac{1}{2}} - z_{i,k\pm\frac{1}{2}}\right)/\Delta x$ with respect to horizontal direction. Eq. (2.2) may be rewritten in flux form as

$$PGF_{i+\frac{1}{2},k} = FX_{i,k} - FX_{i+1,k} + \tag{2.3}$$
$$+FC_{i+\frac{1}{2},k+\frac{1}{2}} - FC_{i+\frac{1}{2},k-\frac{1}{2}}\,,$$

where

$$FX_{i,k} = \int\limits_{z_{i,k-\frac{1}{2}}}^{z_{i,k+\frac{1}{2}}} P\,\mathrm{d}z'\,, \quad FC_{i+\frac{1}{2},k+\frac{1}{2}} = \int\limits_{z_{i,k+\frac{1}{2}}}^{z_{i+1,k+\frac{1}{2}}} P\,\mathrm{d}z'\,. \tag{2.4}$$

Since a second-order discretized hydrostatic equation naturally defines pressure at the vertices of the control-volume element around velocity points,

$$P_{i,k-\frac{1}{2}} = P_{i,N+\frac{1}{2}} + g\sum_{k'=k}^{N} \rho_{i,k'} H_{i,k'}\,; \quad \forall k=1,\,...\,,N \tag{2.5}$$

(where $H_{i,k} = z_{i,k+\frac{1}{2}} - z_{i,k-\frac{1}{2}}$ is the vertical height of the grid box around density $\rho_{i,k}$; $z_{\frac{1}{2}}$ corresponds to the bottom and $z_{N+\frac{1}{2}}$ to the free surface), Lin proposes a

$\overline{\rho}_k$ as a set of grid-box averages,

$$\overline{\rho}_k \equiv \frac{1}{z_{k+\frac{1}{2}} - z_{k-\frac{1}{2}}} \int\limits_{z_{k-\frac{1}{2}}}^{z_{k+\frac{1}{2}}} \rho(z)\mathrm{d}z\,, \tag{3.5}$$

where $\rho(z)$ is a *continuous* density profile. Since on the continuous level pressure $P(z)$ is obtained by vertical integration (1.5), one can verify that after substitution of $\rho_k = \overline{\rho}_k$ into (2.5), the later produces *exact* values of pressure $P_{k-\frac{1}{2}} \equiv P(z_{k-\frac{1}{2}})$. Taking into account that pressure and density are related as a function and its vertical derivative, one can apply the integration rule (3.1) for $FX_{i,k}$ in (2.4) with a cubic fit,

$$FX_{i,k} = \frac{1}{2}H_{i,k}\left[P_{i,k+\frac{1}{2}} + P_{i,k-\frac{1}{2}} + \right. \tag{3.6}$$
$$\left. +gH_{i,k}\frac{\rho_{i,k+\frac{1}{2}} - \rho_{i,k-\frac{1}{2}}}{6}\right],$$

where $H_{i,k} = z_{i,k+\frac{1}{2}} - z_{i,k-\frac{1}{2}}$ and $\rho_{i,k\pm\frac{1}{2}}$ are the values of density at interfaces $z_{i,k\pm\frac{1}{2}}$ between grid boxes $H_{i,k}$ and $H_{i,k\pm1}$. Similarly, application of (3.2) for a quintic fit yields

$$FX_{i,k} = \frac{1}{2}H_{i,k}\left[P_{i,k+\frac{1}{2}} + P_{i,k-\frac{1}{2}} + \right.$$
$$+\frac{1}{5}gH_{i,k}\left(\rho_{i,k+\frac{1}{2}} - \rho_{i,k-\frac{1}{2}} - \right. \tag{3.7}$$
$$\left.\left. -H_{i,k}\cdot\frac{d_{i,k+\frac{1}{2}} + d_{i,k-\frac{1}{2}}}{12}\right)\right],$$

where $d_{i,k\pm\frac{1}{2}}$ are the values of $\frac{\partial\rho}{\partial z}$ at the grid-box interfaces.

Eqs. (3.6) and (3.7) may be derived by an alternative procedure: at every vertical column, for a given set box-averaged values $\left\{\overline{\rho}_i, k \,\middle|\, k = 1, \dots N\right\}$ we *reconstruct* the vertical profile of density field as a continuous function, then use double integration to compute $FX_{i,k}$,

$$FX_{i,k} = \int\limits_{z_{i,k-\frac{1}{2}}}^{z_{i,k+\frac{1}{2}}} \left\{ \int\limits_{z}^{z_{i,N+\frac{1}{2}}} \rho(z')\mathrm{d}z' \right\} \mathrm{d}z\,, \tag{3.8}$$

where the reconstruction [3] algorithm approximates the density distribution inside each grid box H_k by either a quadratic or quartic polynomial, such that it has the same box-averaged value as $\overline{\rho}_k$ and it is continuous (perhaps along with its several derivatives) across grid box interfaces. Once reconstruction is complete, the double integral (3.8) is then computed analytically. We will return to vertical reconstruction algorithms later, but for the rest of this section we assume that $\rho_{k+\frac{1}{2}}$ and $d_{k+\frac{1}{2}}$ are known.

Computation of $FC_{i+\frac{1}{2},k+\frac{1}{2}}$ from (2.4) requires knowledge of derivatives of pressure along the quasi-horizontal coordinates. To compute them we use

$$\left.\frac{\partial P}{\partial x}\right|_{s=\mathrm{const}} = \cos\gamma\cdot\left.\frac{\partial P}{\partial x}\right|_{z=\mathrm{const}} + \sin\gamma\cdot\frac{\partial P}{\partial z}\,, \tag{3.9}$$

where γ is the angle between lines $z = \mathrm{const}$ and $s = \mathrm{const}$ (i.e. coordinate slope), which in the usual small-slope approximation is,

$$\sin\gamma \approx \frac{z_{i+1,k+\frac{1}{2}} - z_{i,k-\frac{1}{2}}}{\Delta x}\,, \qquad \cos\gamma \approx 1\,. \tag{3.10}$$

Taking into account that $\frac{\partial P}{\partial z} = -g\rho$, and using (3.1) for a cubic fit, we arrive at

$$FC_{i+\frac{1}{2},k+\frac{1}{2}} = \frac{1}{2}\Delta z_{i+\frac{1}{2},k+\frac{1}{2}}\left[P_{i+1,k+\frac{1}{2}} + P_{i,k+\frac{1}{2}} + \right.$$
$$+g\Delta z_{i+\frac{1}{2},k+\frac{1}{2}}\frac{\rho_{i+1,k+\frac{1}{2}} - \rho_{i,k+\frac{1}{2}}}{6} - \tag{3.11}$$
$$\left. -\frac{\Delta x}{6}\left(\left.\frac{\partial P}{\partial x}\right|_{\substack{z=\mathrm{const}\\ i+1,k+\frac{1}{2}}} - \left.\frac{\partial P}{\partial x}\right|_{\substack{z=\mathrm{const}\\ i,k+\frac{1}{2}}}\right)\right],$$

where $\Delta z_{i+\frac{1}{2},k+\frac{1}{2}} = z_{i+1,k+\frac{1}{2}} - z_{i,k+\frac{1}{2}}$. We then split $FC_{i+\frac{1}{2},k+\frac{1}{2}}$ into two parts,

$$FC_{i+\frac{1}{2},k+\frac{1}{2}} = FC'_{i+\frac{1}{2},k+\frac{1}{2}} - \frac{\Delta z_{i+\frac{1}{2},k+\frac{1}{2}}\Delta x}{12}\Big(\dots\Big)\,, \tag{3.12}$$

where $FC'_{i+\frac{1}{2},k+\frac{1}{2}}$ contains all terms in the first two lines of (3.11) and terms in braces are the remaining terms. We first neglect the latter and compute a provisional field PGF' using (2.3),

$$PGF'_{i+\frac{1}{2},k} = FX_{i,k} - FX_{i+1,k} + \tag{3.13}$$
$$+FC'_{i+\frac{1}{2},k+\frac{1}{2}} - FC'_{i+\frac{1}{2},k-\frac{1}{2}}\,.$$

In the case of resting stratification, $\left.\frac{\partial P}{\partial x}\right|_{z=\mathrm{const}}$ vanishes, and no error is associated with neglecting these terms, leaving the remaining hydrostatic consistency error due to only reconstruction and integration errors.

In the case when quintic integration rule is used to compute $FX_{i,k}$ (i.e., (3.7) instead of (3.6)), $FC'_{i+\frac{1}{2},k+\frac{1}{2}}$

[3] The mathematical term *reconstruction* (as opposite to interpolation) is used here to emphasize that the input data $\overline{\rho}_k$ exists only in sense of grid-box averages. Thus, it no longer makes sense to say that density is specified at a given grid levels, and the goal here is to obtain its values at locations between.

in the sense that term on the right is second order with respect to the term on the left[4]. Therefore, it is established that the difference between $PGF'_{i+\frac{1}{2},k}$ and $PGF_{i+\frac{1}{2},k}$ is second order accurate with respect to either one. The nondimensional factor r in (3.24) is the ratio of vertical increment over one horizontal grid interval due to slope of quasi-horizontal coordinates and vertical grid spacing:

$$r = \frac{z_{i+1,k+\frac{1}{2}} - z_{i,k+\frac{1}{2}} + z_{i+1,k-\frac{1}{2}} - z_{i,k-\frac{1}{2}}}{z_{i+1,k+\frac{1}{2}} - z_{i+1,k-\frac{1}{2}} + z_{i,k+\frac{1}{2}} - z_{i,k-\frac{1}{2}}}\,. \qquad (3.25)$$

This factor is sometimes known as "hydrostatic consistency" criterion of the grid (e.g., Janjic, 1977; Mahrer, 1884; Haney, 1991). Specifically, grids with $r \leq 1$ are often referred as hydrostatically consistent, while $r > 1$ are hydrostatically inconsistent. We believe that there is no "sharp" barrier associated with exceeding $r > 1$ (like the CFL criterion for time stepping stability); however, it is clear that the accuracy of the algorithm deteriorates with increasing r.

We propose the following procedure for correction of the dynamical error due to the missing terms (3.22):

1. Compute $PGF'_{i+\frac{1}{2},k}$ as described above;
2. Compute $PX_{i+\frac{1}{2},k}$ using (3.23), except $PGF'_{i+\frac{1}{2},k}$ is used instead of $PGF_{i+\frac{1}{2},k}$;
3. Compute $PX_{i,k+\frac{1}{2}}$ from $PX_{i+\frac{1}{2},k}$ using slope-dependent interpolation by (3.26) below; then compute the correction terms (3.22) and add them to $PGF'_{i+\frac{1}{2},k}$, which is then accepted as the final version of $PGF_{i+\frac{1}{2},k}$.

Since this error correction does not involve the stiff balance in (1.1)-(1.4), the requirements for its accuracy are milder than for the computation of $PGF'_{i+\frac{1}{2},k}$.

The slope-dependent interpolation used in step 3 is

$$\begin{aligned} FC''_{i+\frac{1}{2},k+\frac{1}{2}} = \max\left(0.,\, z_{i+1,k+\frac{1}{2}} - z_{i,k+\frac{1}{2}}\right) \times \\ \times \Big[PX_{i+\frac{1}{2},k+1} + PX_{i+\frac{3}{2},k} - \\ -PX_{i-\frac{1}{2},k+1} - PX_{i+\frac{1}{2},k}\Big] \qquad (3.26) \\ +\min\left(0.,\, z_{i+1,k+\frac{1}{2}} - z_{i,k+\frac{1}{2}}\right) \times \\ \times \Big[PX_{i+\frac{1}{2},k} + PX_{i+\frac{3}{2},k+1} - \\ -PX_{i-\frac{1}{2},k} - PX_{i+\frac{1}{2},k+1}\Big]\,, \end{aligned}$$

where the use of a 2-point diagonal stencil in (3.26) to obtain $PX_{i,k+\frac{1}{2}}$ from $PX_{i+\frac{1}{2},k}$ rather than a more standard 4-point one is motivated by the desire to restrict the size of the stencil in vertical direction. If the procedure described here is continued iteratively, it converges toward compact approximation for horizontal derivatives. Stability of iteration imposes the restriction $r < 3$ (see Appendix B).

The overall description of the algorithm to compute pressure gradient force is now complete, provided that the interfacial densities $\rho_{k+\frac{1}{2}}$ and vertical derivatives $d_{k+\frac{1}{2}}$ are known. These interfacial values are obtained at each vertical column from vertical averages $\overline{\rho}_k$ using one of the reconstruction algorithms which will be described in the next section.

4. Reconstruction Algorithms

4.1. Preliminary Remarks

Although the problem of finding interfacial values and derivatives from the set of grid-box averages is very common in computational fluid mechanics (e.g., in the context of conservation laws), almost none of the previously known algorithms can be applied directly for the purpose of computation of pressure gradient force. As we will show in this section, the main obstacle is that it is not sufficient just to find interfacial values using a high-order interpolation scheme. Instead we have to focus our attention on the behavior of the interpolant as a *continuos* function, which is crucial for the accurate evaluation of the integrals (3.6)–(3.11) or (3.7)–(3.14) and eventually for the hydrostatic error of the pressure gradient scheme. Hence, for our purposes, it is natural to judge the accuracy of a reconstruction algorithm by the continuous quadratic measure,

$$\epsilon = \sqrt{\frac{1}{D}\int_{z_{\rm bot}}^{z_{\rm surf}} \left[\mathcal{R}(z) - \rho_{\rm exact}(z)\right]^2 {\rm d}z}\,, \qquad (4.1)$$

where $\mathcal{R}(z)$ and $\rho_{\rm exact}(z)$ are the reconstructed and exact densities respectively, and $D = z_{\rm surf} - z_{\rm bot}$ is the total depth of water column.

Since the only known information about the density field is the set of grid-box values, any reconstruction algorithm involves certain degree of speculation about the behavior of the continuous field, e.g., continuity, smoothness (including continuity of higher-order derivatives), mono-

[4]The correction terms (3.22) are the part of the truncation error of the Lin's scheme. Their smallness in (3.24) is simply a consequence of the fact that Lin's scheme is second-order accurate.

Linear extrapolation rule, [equivalent to setting $d_{\frac{1}{2}} = d_{\frac{3}{2}}$ and $d_{N+\frac{1}{2}} = d_{N-\frac{1}{2}}$ in terms of Eqs. (4.2)–(4.9)]:

$$\rho_{\frac{1}{2}} + \rho_{\frac{3}{2}} = 2\overline{\rho}_1\,, \qquad \rho_{N+\frac{1}{2}} + \rho_{N-\frac{1}{2}} = 2\overline{\rho}_N\,. \qquad (4.12)$$

Quadratic extrapolation rule [assumption that the second derivative within the grid box adjacent to the boundary is the same as in the grid next to it from inside]:

$$\begin{aligned} H_2\rho_{\frac{1}{2}} + \big(H_1+H_2\big)\rho_{\frac{3}{2}} &= \frac{H_2\big(2H_2+3H_1\big)}{H_1+H_2}\overline{\rho}_1 \\ &\qquad + \frac{H_1^2}{H_1+H_2}\overline{\rho}_2\,, \\ \big(H_N+H_{N-1}\big)\rho_{N-\frac{1}{2}} + H_{N-1}\rho_{N+\frac{1}{2}} & \qquad\qquad (4.13) \\ = \frac{H_{N-1}\big(2H_{N-1}+3H_N\big)}{H_N+H_{N-1}}\overline{\rho}_N &+ \\ + \frac{H_N^2}{H_N+H_{N-1}}\overline{\rho}_{N-1}\,. & \end{aligned}$$

Eqs. (4.9) along with an appropriate set of boundary condition comprise a well posed (diagonally dominant) system and its resolution is straightforward.

For a test problem we setup a nonuniform grid generated by a mapping function commonly used in ocean modeling practice, Song & Haidvogel, 1994,

$$z_{k+\frac{1}{2}} = h_{\rm c}\sigma_{k+\frac{1}{2}} + \big(h-h_{\rm c}\big)\frac{\sinh(\theta\sigma_{k+\frac{1}{2}})}{\sinh(\theta)}\,, \qquad (4.14)$$

where $\sigma_{k+\frac{1}{2}} \equiv (N-k)/N$, so that $-1 \le \sigma_{k+\frac{1}{2}} \le 0$, $k = 0, \dots N$. For illustrations below we set in (4.14) $\theta = 7$, $h = 3000$ and $h_{\rm c} = 200$. We also chose an analytical profile,

$$\rho(z) = \tanh\left(\frac{z-z_C}{\delta}\right)\,, \qquad (4.15)$$

where $-3000 < z < 0$, $z_C = -450$ and $\delta = 150$. The grid-box values are then obtained by analytical integration of(4.15) [e.g. Gradshteyn & Ryzhik, 1965],

$$\begin{aligned} \overline{\rho}_k &= \frac{1}{z_{k+\frac{1}{2}} - z_{k-\frac{1}{2}}}\int\limits_{z_{k-\frac{1}{2}}}^{z_{k+\frac{1}{2}}} \tanh\left(\frac{z-z_C}{\delta}\right){\rm d}z = \qquad (4.16) \\ &= \frac{\delta}{z_{k+\frac{1}{2}} - z_{k-\frac{1}{2}}}\ln\left(\frac{\cosh\Big(\big(z_{k+\frac{1}{2}}-z_C\big)/\delta\Big)}{\cosh\Big(\big(z_{k-\frac{1}{2}}-z_C\big)/\delta\Big)}\right)\,, \end{aligned}$$

$k = 1, \dots, N$. Once the set of $\overline{\rho}_k$ is computed, it becomes the only information spline reconstruction algorithm "knows" about the profile.

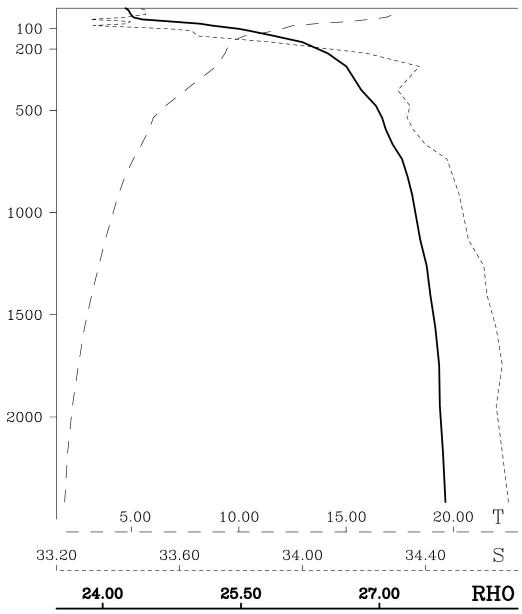

Figure 3. An example of typical profiles of temperature (*in situ*), salinity, and potential density (with effect of compressibility removed and $\rho_0 = 1000$ subtracted). These profiles are measured within CalCOFFI domain off the California coast. Courtesy of John Moisan.

The use of tanh profiles for the example is motivated by the typical oceanic vertical structure of temperature, salinity and density (see Fig. 3). It features a quasi-uniform layer near the surface due to enhanced mixing, a main thermocline, and a thick weakly stratified abyssal region. Fig. 3 also illustrates highly nonuniform scales of vertical variation in all three fields, which strongly motivates the use of nonuniform grid spacing in (4.14).

The reconstructed profiles are shown in Fig. 4. The fifteen curves on each panel from left to right correspond to vertical resolution of $N = 7, \dots 21$ where N is the number of grid boxes of a nonuniform grid. Tickmarks indicate interfaces between the grid boxes, while vertical straight line in each box corresponds to the box-averaged values. This example shows fast convergence of the reconstructed profile toward analytical one with increase of vertical resolution, but at the same time significant oscillations are present with coarse resolution. This Fig. also shows sensitivity to the boundary conditions.

4.3. Basic Quartic Spline

Alternatively to (4.2), now we approximate the density distribution by a quartic polynomial,

$$\rho(z') = A_k {z'}^4 + B_k {z'}^3 + C_k {z'}^2 + D_k z' + E_k \quad , \tag{4.17}$$

where, once again, z' is local coordinate within the grid box H_k. The coefficients A_k, B_k, C_k, D_k, E_k, $k = 1,..,N$ will be chosen in such a way that (4.17) has the grid-box-averaged value of $\overline{\rho}_k$ and the interpolant is continuous across the grid box interfaces along with its first, second and third derivatives.

To achieve this goal, we first introduce a new set of unknowns, $\{\rho_{k+\frac{1}{2}}\,,\; d_{k+\frac{1}{2}}\,|\, k = 0,...,N\}$, which are the interfacial values of density and its vertical derivatives, and express (4.17) in terms of these new variables, rather than power coefficients A_k, B_k, C_k, D_k, E_k. Integration of (4.17) within the grid-box yields

$$\overline{\rho}_k \equiv \frac{1}{H_k} \int\limits_{-H_k/2}^{+H_k/2} \rho(z')\, dz' = \frac{A_k H_k^4}{80} + \frac{C_k H_k^2}{12} + E_k \,, \tag{4.18}$$

while substitution of $z' = \pm H_k/2$ into (4.17) results in the interfacial values,

$$\rho_{k\pm\frac{1}{2}} \equiv \rho\left(\pm\frac{H_k}{2}\right) = \frac{A_k H_k^4}{16} + \frac{C_k H_k^2}{4} + E_k \pm \pm\left(\frac{B_k H_k^3}{8} + \frac{D_k H_k}{2}\right) , \tag{4.19}$$

and the interfacial derivatives,

$$d_{k\pm\frac{1}{2}} \equiv \frac{\partial \rho}{\partial z'}\Big|_{z'=\pm H_k/2} = \pm\left(\frac{A_k H_k^3}{2} + C_k H_k\right) + +\frac{3 B_k H_k^2}{4} + D_k \,. \tag{4.20}$$

As an immediate consequence from (4.19) and (4.20),

$$\frac{A_k H_k^4}{16} + \frac{C_k H_k^2}{4} + E_k = \frac{\rho_{k+\frac{1}{2}} + \rho_{k-\frac{1}{2}}}{2} \,, \tag{4.21}$$

$$A_k H_k^3 + 2 C_k H_k = d_{k+\frac{1}{2}} - d_{k-\frac{1}{2}} \,, \tag{4.22}$$

$$\frac{B_k H_k^3}{4} + D_k H_k = \rho_{k+\frac{1}{2}} - \rho_{k-\frac{1}{2}} \,, \tag{4.23}$$

$$\frac{3 B_k H_k^2}{4} + D_k = \frac{d_{k+\frac{1}{2}} + d_{k-\frac{1}{2}}}{2} \,, \tag{4.24}$$

which together with the integral consistency condition (4.18) comprise the system of five equations needed to express the coefficients A_k, B_k, C_k, D_k, E_k in terms of $\overline{\rho}_k$, $\rho_{k\pm\frac{1}{2}}$, $d_{k\pm\frac{1}{2}}$ and eventually leads to an alternative representation of (4.17),

$$\begin{aligned} \rho(z') = \overline{\rho}_k - \frac{7}{8}\left(\frac{\rho_{k+\frac{1}{2}} + \rho_{k-\frac{1}{2}}}{2} - \overline{\rho}_k\right) + & \\ + \frac{1}{32}(d_{k+\frac{1}{2}} - d_{k-\frac{1}{2}}) H_k & \\ + \left[\frac{3}{2}(\rho_{k+\frac{1}{2}} - \rho_{k-\frac{1}{2}}) - \frac{1}{4}(d_{k+\frac{1}{2}} + d_{k-\frac{1}{2}}) H_k\right] \frac{z'}{H_k} & \\ + \left[15\left(\frac{\rho_{k+\frac{1}{2}} + \rho_{k-\frac{1}{2}}}{2} - \overline{\rho}_k\right) - \right. & \\ \left. - \frac{3}{4}(d_{k+\frac{1}{2}} - d_{k-\frac{1}{2}}) H_k\right] \frac{{z'}^2}{H_k^2} & \\ + \left[(d_{k+\frac{1}{2}} + d_{k-\frac{1}{2}}) H_k - 2(\rho_{k+\frac{1}{2}} - \rho_{k-\frac{1}{2}})\right] \frac{{z'}^3}{H_k^3} & \\ + \left[\frac{5}{2}(d_{k+\frac{1}{2}} - d_{k-\frac{1}{2}}) H_k - \right. & \\ \left. -30\left(\frac{\rho_{k+\frac{1}{2}} + \rho_{k-\frac{1}{2}}}{2} - \overline{\rho}_k\right)\right] \frac{{z'}^4}{H_k^4} \,. & \end{aligned} \tag{4.25}$$

Since $\rho_{k+\frac{1}{2}}$ and $d_{k+\frac{1}{2}}$ are shared between the adjacent grid boxes, the form of (4.25) already guarantees that the interpolant and its first derivative are continuous across the grid box interfaces. Values of $\rho_{k+\frac{1}{2}}$ and $d_{k+\frac{1}{2}}$ are then determined from the continuity conditions for the second and the third derivatives. To derive these conditions, we note that

$$\frac{\partial^2 \rho}{\partial {z'}^2}\Bigg|_{z'=+H_k/2} = \frac{-36\rho_{k+\frac{1}{2}} - 24\rho_{k-\frac{1}{2}} + 60\overline{\rho}_k}{H_k^2} + + \frac{9 d_{k+\frac{1}{2}} - 3 d_{k-\frac{1}{2}}}{H_k} \tag{4.26}$$

$$\frac{\partial^2 \rho}{\partial {z'}^2}\Bigg|_{z'=-H_k/2} = \frac{-24\rho_{k+\frac{1}{2}} - 36\rho_{k-\frac{1}{2}} + 60\overline{\rho}_k}{H_k^2} + + \frac{3 d_{k+\frac{1}{2}} - 9 d_{k-\frac{1}{2}}}{H_k} \,. \tag{4.27}$$

The matching condition for the second derivatives is therefore derived by incrementing index k in (4.27) by 1 and equating the result to (4.26),

$$\begin{aligned} -\frac{2}{5}\frac{\rho_{k-\frac{1}{2}}}{H_k^2} + \frac{3}{5}\left(\frac{1}{H_{k+1}^2} - \frac{1}{H_k^2}\right)\rho_{k+\frac{1}{2}} + \frac{2}{5}\frac{\rho_{k+\frac{3}{2}}}{H_{k+1}^2} - & \\ -\frac{d_{k-\frac{1}{2}}}{20 H_k} + \frac{3}{20}\left(\frac{1}{H_{k+1}} + \frac{1}{H_k}\right) d_{k+\frac{1}{2}} - \frac{d_{k+\frac{3}{2}}}{20 H_{k+1}} = & \\ = \frac{\overline{\rho}_{k+1}}{H_{k+1}^2} - \frac{\overline{\rho}_k}{H_k^2} \,, & \end{aligned} \tag{4.28}$$

Therefore,

$$\mathbf{C}_{k+\frac{1}{2}} = \mathbf{B}'_{k+\frac{1}{2}} \cdot \mathbf{A}'_{k+1} \tag{4.41}$$

$$\mathbf{d}^*_{k+\frac{1}{2}} = \mathbf{B}'_{k+\frac{1}{2}} \cdot \left(\mathbf{d}_{k+\frac{1}{2}} - \mathbf{A}_k \cdot \mathbf{d}^*_{k-\frac{1}{2}}\right) , \tag{4.42}$$

$$\text{where} \quad \mathbf{B}'_{k+\frac{1}{2}} = \left(\mathbf{B}_{k+\frac{1}{2}} - \mathbf{A}_k \cdot \mathbf{C}_{k-\frac{1}{2}}\right)^{-1} , \tag{4.43}$$

and -1 indicates operation of matrix inverse, which is quite trivial for a 2×2 matrix, e.g.,

$$\mathbf{B} = \begin{pmatrix} b_{11} & b_{12} \\ b_{21} & b_{22} \end{pmatrix} \quad \Rightarrow \quad \mathbf{B}^{-1} = \frac{1}{\Delta} \begin{pmatrix} b_{22} & -b_{12} \\ -b_{21} & b_{11} \end{pmatrix} \tag{4.44}$$

$$\text{where} \qquad \Delta = b_{11}b_{22} - b_{12}b_{21} \, .$$

This completes the description of forward elimination algorithm.

Once (4.41)–(4.43) reaches $k = N - 1$, the remaining sub-system,

$$\mathbf{r}_{N-\frac{1}{2}} + \mathbf{C}_{N-\frac{1}{2}} \cdot \mathbf{r}_{N+\frac{1}{2}} = \mathbf{d}^*_{N-\frac{1}{2}} \tag{4.45}$$

$$\mathbf{C}'_{N+\frac{1}{2}} \cdot \mathbf{r}_{N-\frac{1}{2}} + \mathbf{r}_{N+\frac{1}{2}} = \mathbf{d}_{N+\frac{1}{2}} , \tag{4.46}$$

needs to be solved directly for $\mathbf{r}_{N+\frac{1}{2}}$. In (4.46), which is the matrix form of top boundary condition, $\mathbf{C}'_{N+\frac{1}{2}}$ is similar in structure to $\mathbf{C}_{\frac{1}{2}}$, which will be discussed below. Note that $\mathbf{C}'_{N+\frac{1}{2}}$ in (4.46) is primed to distinguish it from regular $\mathbf{C}_{k+\frac{1}{2}}$, since it has different usage: it is applied to the element on the left of the diagonal element, rather than on the right.

After $\mathbf{r}_{N+\frac{1}{2}}$ is known, the remaining all $\mathbf{r}_{k+\frac{1}{2}}$, $k = N - 1, \ldots 0$ are computed sequentially via a backward sweep,

$$\mathbf{r}_{k+\frac{1}{2}} = \mathbf{d}^*_{k+\frac{1}{2}} - \mathbf{C}_{k+\frac{1}{2}} \cdot \mathbf{r}_{k+\frac{3}{2}} , \tag{4.47}$$

which completes the solution.

Finally, we have to describe boundary conditions for (4.38) and (4.46). Two boundary conditions are required on each side, which, similarly to the case of parabolic splines, may be either physically motivated or purely numerical.

Plausible choices are the following:

Neumann: the first derivative vanishes on the boundary,

$$d_{\frac{1}{2}} = 0 \, . \tag{4.48}$$

Taken alone, this condition is not sufficient, since it restricts only one unknown. To provide the second condition, one can restrict the power polynomial to the third in the bottom most grid box by setting the last coefficient in (4.25) to zero,

$$\frac{5}{2}(d_{\frac{3}{2}} - d_{\frac{1}{2}})H_1 - 30\left(\frac{\rho_{\frac{3}{2}} + \rho_{\frac{1}{2}}}{2} - \overline{\rho}_1\right) = 0 \, . \tag{4.49}$$

Eqs. (4.48)—(4.49) may be reformulated in matrix form,

$$\mathbf{C}_{\frac{1}{2}} = \begin{pmatrix} 1 & -\frac{H_1}{6} \\ 0 & 0 \end{pmatrix} \qquad \mathbf{d}^*_{\frac{1}{2}} = \begin{pmatrix} 2\overline{\rho}_1 \\ 0 \end{pmatrix} , \tag{4.50}$$

which then are substituted in (4.38). Similarly at top (4.46), matrix $\mathbf{C}_{N+\frac{1}{2}}$ and vector $\mathbf{d}^*_{N+\frac{1}{2}}$ are obtained by the setting

$$d_{N+\frac{1}{2}} = 0 \tag{4.51}$$

and

$$30\left(\frac{\rho_{N+\frac{1}{2}} + \rho_{N-\frac{1}{2}}}{2} - \overline{\rho}_N\right) - \tag{4.52}$$
$$-\frac{5}{2}(d_{N+\frac{1}{2}} - d_{N-\frac{1}{2}})H_N = 0 \, ,$$

which leads to

$$\mathbf{C}'_{N+\frac{1}{2}} = \begin{pmatrix} 1 & +\frac{H_N}{6} \\ 0 & 0 \end{pmatrix} \qquad \mathbf{d}_{N+\frac{1}{2}} = \begin{pmatrix} 2\overline{\rho}_N \\ 0 \end{pmatrix} . \tag{4.53}$$

Parabolic truncation: Suppose that there is no physical justification for (4.48), or any other physical B.C. Then, one can simply restrict the order of the polynomial to second in the bottom-most grid box. Thus, in insted of (4.48) one can use

$$(d_{\frac{2}{2}} + d_{\frac{1}{2}})H_1 - 2(\rho_{\frac{3}{2}} - \rho_{\frac{1}{2}}) = 0 \, , \tag{4.54}$$

which is used in combination with with (4.49). The corresponding matrix form is

$$\mathbf{C}_{\frac{1}{2}} = \begin{pmatrix} 2 & -\frac{H_1}{2} \\ -\frac{6}{H_1} & 2 \end{pmatrix} \qquad \mathbf{d}_{\frac{1}{2}} = \begin{pmatrix} 3\overline{\rho}_1 \\ -\frac{6\overline{\rho}_1}{H_1} \end{pmatrix} . \tag{4.55}$$

Similarly at the top,

$$(d_{N+\frac{1}{2}} + d_{N-\frac{1}{2}})H_N - 2(\rho_{N+\frac{1}{2}} - \rho_{N-\frac{1}{2}}) = 0 \, , \tag{4.56}$$

which in combination with (4.52) results in

$$\mathbf{C}'_{N+\frac{1}{2}} = \begin{pmatrix} 2 & +\frac{H_N}{2} \\ +\frac{6}{H_N} & 2 \end{pmatrix} \qquad \mathbf{d}^*_{N+\frac{1}{2}} = \begin{pmatrix} 3\overline{\rho}_N \\ \frac{6\overline{\rho}_N}{H_N} \end{pmatrix} . \tag{4.57}$$

Fig. 5 shows profiles reconstructed by quartic splines for the test problem (4.14)—(4.15). In comparison with parabolic splines, quartic algorithm has faster convergence (which will be shown later), but overall at this resolution there is no obvious advantage of quartic splines in comparison with parabolic: in both cases, once $N \geq 20$, there is no visible difference between the reconstructed and analytical profiles. At coarse resolution, going from parabolic to quartic splines makes the problem of oscillations worse, which is not unusual behaviour high-order interpolants. Quartic spline are also somewhat less sensitive to the choice of boundary conditions than parabolic. Clearly thus far, neither parabolic, nor quartic spline provide reconstruction algorithm sufficiently robust enough to avoid potential for hydrostatic instability at coarse resolution and sharp thermocline.

Computational cost and storage requirements: Overall, quartic spline reconstruction requires only 2 divisions for each grid box ($1/H_k$ to compute elements of $\mathbf{A}_k$ and $1/\Delta$ during matrix inversion, (4.43)) and approximately 40 additions and multiplications, which makes it 2.5 times more expensive than basic parabolic spline algorithm. The relatively high operation count of the quartc algorithm is mitigated by the fact that all operations associated with matrix-matrix and matrix-vector products are naturally arranged in multiply-add sequences with each operand participating in at least two mathematical operations, thus resulting in optimal computational density of the code. It should be also mentioned that in the context of a three-dimensional problem this algorithm is fully vectorizable, since the operations can be arranged in X-Z planes with innermost sweeps in horizontal direction.

It should be noted that since matrices $\mathbf{B}_{k+\frac{1}{2}}$ and $\mathbf{B}'_{k+\frac{1}{2}}$ are not needed before or after (4.41)–(4.43), and since $\mathbf{B}_{k+\frac{1}{2}}$ is computed from $\mathbf{A}$ via (4.35), there is no need to store $\mathbf{B}$ or $\mathbf{B}'$ in scratch arrays. Also, if $\mathbf{C}_{k+\frac{1}{2}}$ is aligned in computer memory with $\mathbf{A}_k$, scratch arrays for $\mathbf{A}$ may be overwritten by $\mathbf{C}$, because once $\mathbf{C}_{k+\frac{1}{2}}$ is computed, there is no longer need to keep $\mathbf{A}_k$ (recall that $\mathbf{C}_{k+\frac{1}{2}}$ depends on $\mathbf{A}_k$ (which participates in $\mathbf{B}_{k+\frac{1}{2}}$) and $\mathbf{A}_{k+1}$ in (4.41)–(4.43)). It is also obvious that $\mathbf{r}_{k+\frac{1}{2}}$, $\mathbf{d}_{k+\frac{1}{2}}$ and $\mathbf{d}^*_{k+\frac{1}{2}}$ may be stored in the same arrays, since they are not needed simultaneously in the algorithm described above. Therefore, the algorithm described above requires only 4 scratch arrays of length $N+1$ to hold elements of matrices $\mathbf{A}$ (same as $\mathbf{C}$; +1 due to index shift) and 2 arrays of the same size to hold $\mathbf{r}$.

4.4. Piecewise Parabolic Method

Next we discuss reconstruction algorithms based on local polynomial fit. The attractiveness of these methods is due to the fact that unlike splines, they allow incorporation of monotonicity constraints which suppress spurious oscillations.

In the Piecewise Parabolic Method (PPM), Colella & Woodward, 1984, the interfacial values are $\rho_{k+\frac{1}{2}}$ are obtained by fitting a cubic polynomial such that its integrals over grid boxes H_{k-1}, H_k, H_{k+1} and H_{k+2} are equal to $\rho_{k-1}H_{k-1}$, $\rho_k H_k$, $\rho_{k+1}H_{k+1}$ and $\rho_{k+2}H_{k+2}$ respectively[5]. After that it is assumed that the distribution in each gridbox is given by parabolic segment similar to (4.2). The PPM monotonization procedure consists of slope limiting [given by Eq (1.8) in Colella & Woodward, 1984] which in effect restricts interpolation across grid boxes where there are sharp changes of the slope, specifically if consecutive differences $\rho_{k+1} - \rho_k$ and $\rho_k - \rho_{k-1}$ differ by more than a factor of 4 in the case of a uniform grid, or a ratio dependent on local grid spacing in the case of nonuniform. This procedure also forces $\rho_{k+\frac{1}{2}}$ to be within the bounds of $\min, \max(\rho_k, \rho_{k+1})$. Then, inside each grid box, the parabolic segments are constrained in such a way that the extremum always lies outside the box. To do so we adopt an algorithm,

$$
\begin{array}{lll}
\text{assign:} & \begin{array}{l} \delta_k^R = \rho_{k+\frac{1}{2}} - \overline{\rho}_k \\ \delta_k^L = \overline{\rho}_k - \rho_{k-\frac{1}{2}} \end{array} & \\[2ex]
\text{reject:} & \begin{array}{l} \delta_k^R = 0 \\ \delta_k^L = 0 \end{array} & \text{if} \quad \delta_k^R \cdot \delta_k^L < 0 \\[2ex]
\text{restrict:} & \begin{array}{l} \delta_k^R = 2\delta_k^L\,, \\ \delta_k^L = 2\delta_k^R\,, \end{array} & \begin{array}{l} \text{if} \quad |\delta_k^R| > 2|\delta_k^L| \\ \text{if} \quad |\delta_k^L| > 2|\delta_k^R| \end{array} \\[2ex]
\text{assign:} & \begin{array}{l} \rho_k^R = \overline{\rho}_k + \delta_k^R \\ \rho_k^L = \overline{\rho}_k - \delta_k^L \end{array} &
\end{array}
\tag{4.58}
$$

which is equivalent to Eq. (1.10) in Colella & Woodward, 1984, despite its somewhat simpler appearance. Meaning of all variables, $\rho_k^{L,R}$, $\delta_k^{L,R}$, etc. as well as the effect of monotonization procedure (4.58) is explained in Fig. 6 .

After application of (4.58), the parabolic segment (4.2) becomes

$$
\rho(z') = \rho_k^R \left(\frac{1}{2} + \frac{z'}{H_k} \right) + \rho_k^L \left(\frac{1}{2} - \frac{z'}{H_k} \right) \tag{4.59}
$$

[5]This is equivalent to the quartic polynomial fit for indefinite integral of density, as it was described in Colella & Woodward, 1984.

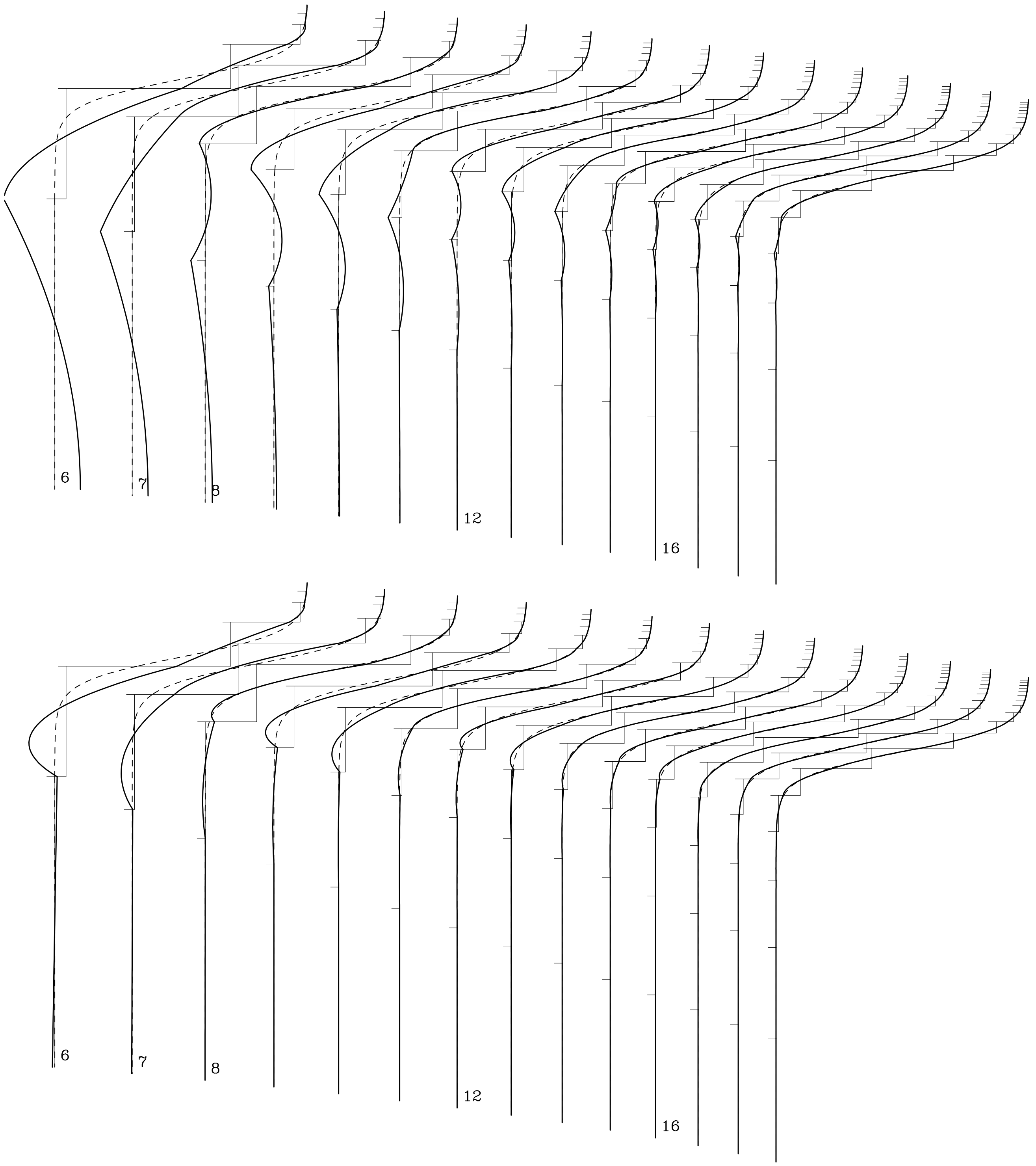

Figure 7. Vertical profiles reconstructed by PPM. **Upper panel** — without limiters; **Lower panel** — with slope limiters only [i.e. Eq. (1.8) in Colella & Woodward (1984) is applied, but the internal monotonicity constraint (1.10) is not].

polants based on four fixed points each,

$$\begin{array}{llll} \mathcal{P}_{k+1} = & \overline{\rho}_{k+1}H_{k+1} + \overline{\rho}_{k+2}H_{k+2} & & z'' = H_{k+1}+H_{k+2} \\ \mathcal{P}_{k+1} = & \mathcal{P}_k = \overline{\rho}_{k+1}H_{k+1} & & z'' = H_{k+1} \\ \mathcal{P}_{k+1} = & \mathcal{P}_k = 0 & & z'' = 0 \\ \mathcal{P}_{k+1} = & \mathcal{P}_k = -\overline{\rho}_k H_k & & z'' = -H_k \\ & \mathcal{P}_k = -\overline{\rho}_k H_k - \overline{\rho}_{k-1}H_{k-1} & & z'' = -H_k - H_{k-1} \end{array}$$

so that $\mathcal{Q}(z'')$ passes through all five fixed points[6]. (Recall that $\mathcal{P}_k\,(H_{k+1}+H_{k+2})$ and $\mathcal{P}_{k+1}\,(-H_k - H_{k-1})$ are not specified above.) The interfacial value $\rho_{k+\frac{1}{2}}$ and, in principle, interfacial derivative $d_{k+\frac{1}{2}}$ may be then determined by

$$\rho_{k+\frac{1}{2}} = \left.\frac{\partial \mathcal{Q}}{\partial z''}\right|_{z''=0} \qquad d_{k+\frac{1}{2}} = \left.\frac{\partial^2 \mathcal{Q}}{\partial z''^2}\right|_{z''=0} \tag{4.64}$$

or simply

$$\begin{aligned} \rho_{k+\frac{1}{2}} &= \frac{\rho_k^R(H_{k+1}+H_{k+2}) + \rho_{k+1}^L(H_k + H_{k-1})}{H_{k-1}+H_k+H_{k+1}+H_{k+2}} \\ d_{k+\frac{1}{2}} &= \frac{d_k^R(H_{k+1}+H_{k+2}) + d_{k+1}^L(H_k + H_{k-1})}{H_{k-1}+H_k+H_{k+1}+H_{k+2}} \\ &\qquad + \frac{2(\rho_{k+1}^L - \rho_k^R)}{H_{k-1}+H_k+H_{k+1}+H_{k+2}} \end{aligned} \tag{4.65}$$

where

$$\begin{aligned} \rho_k^R &= \left.\frac{\partial \mathcal{P}_k}{\partial z''}\right|_{z''=0} \equiv \mathcal{R}_k\Big|_{z''=0} \\ \rho_{k+1}^L &= \left.\frac{\partial \mathcal{P}_{k+1}}{\partial z''}\right|_{z''=0} \equiv \mathcal{R}_{k+1}\Big|_{z''=0} \end{aligned} \tag{4.66}$$

are the right and left side values of density field obtained from the parabolic distributions $\mathcal{R}_k(z'')$ and $\mathcal{R}_{k+1}(z'')$ within the corresponding grid boxes. Similarly,

$$d_k^R = \left.\frac{\partial \mathcal{R}_k}{\partial z''}\right|_{z''=0} \qquad d_{k+1}^L = \left.\frac{\partial \mathcal{R}_{k+1}}{\partial z''}\right|_{z''=0} \tag{4.67}$$

are the right and left side values of density derivatives.

The problem is therefore reduces to reconstruction of $\rho(z')$ inside each grid box H_k using three nearest grid-box averaged values, $\overline{\rho}_{k-1}$, $\overline{\rho}_k$, $\overline{\rho}_{k+1}$ and assuming that $\rho(z)$ is given by a parabolic profile inside H_k. In the unlimited version of this procedure, we first compute elementary half-slopes at every grid box interface,

$$d^{(0)}_{k+\frac{1}{2}} = \frac{\overline{\rho}_{k+1} - \overline{\rho}_k}{H_{k+1}+H_k}\,, \tag{4.68}$$

[6] Here we use notation z'' for local coordinate to avoid confusion with z', cf. (4.59). z'' has its origin at the interface $z_{k+\frac{1}{2}}$, while z' has its origin in the middle of grid box H_k

then compute side deviations for density distribution within grid box H_k,

$$\begin{aligned} \delta_k^R &= H_k\left(d^{(0)}_{k+\frac{1}{2}} - H_{k+1}\gamma_k\right) \\ \delta_k^L &= H_k\left(d^{(0)}_{k-\frac{1}{2}} + H_{k-1}\gamma_k\right) \end{aligned} \tag{4.69}$$

where

$$\gamma_k = \frac{d^{(0)}_{k+\frac{1}{2}} - d^{(0)}_{k-\frac{1}{2}}}{H_{k+1}+H_k+H_{k-1}}\,,$$

then compute side values and derivatives

$$\begin{aligned} \rho_k^R &= \overline{\rho}_k + \delta_k^R \qquad & d_k^R &= \left(4\delta_k^R - 2\delta_k^L\right)/\,H_k \\ \rho_k^L &= \overline{\rho}_k - \delta_k^L \qquad & d_k^L &= \left(4\delta_k^L - 2\delta_k^R\right)/\,H_k \end{aligned} \tag{4.70}$$

which, if substituted into (4.59), produce parabolic fit for $\rho(z')$, such that its grid-box averages over grid boxes H_{k-1}, H_k and H_{k+1} are *exactly* equal to $\overline{\rho}_{k-1}$, $\overline{\rho}_k$ and $\overline{\rho}_{k+1}$ respectively.

Once $\rho_k^{L,R}$ and $d_k^{L,R}$ are known for all grid boxes H_k, the interfacial values and derivatives are then computed via (4.65). By its design the resultant polynomial fit is *exact* if $\rho(z) = z$, z^2, z^3 and any linear combination thereof *regardless* of the non-uniformity of vertical grid. Thus far this prodedure is equivalent to the unlimited version of Eqs. (1.6)–(1.7) from Colella & Woodward, 1984[7].

Now we introduce limiting into (4.69)–(4.70). We need to enforce that

$$\begin{aligned} \min\left(\overline{\rho}_k, \overline{\rho}_{k+1}\right) \le \rho_k^R \le \max\left(\overline{\rho}_k, \overline{\rho}_{k+1}\right) \\ \min\left(\overline{\rho}_{k-1}, \overline{\rho}_k\right) \le \rho_k^L \le \max\left(\overline{\rho}_{k-1}, \overline{\rho}_k\right) \end{aligned} \tag{4.71}$$

and we also require monotonicity of the parabola within the grid box H_k. One should note that δ_k^R and δ_k^L are *convex* combinations of $d^{(0)}_{k+\frac{1}{2}}$ and $d^{(0)}_{k-\frac{1}{2}}$, since (4.69) may be rewritten in form

$$\begin{aligned} \delta_k^R &= H_k\frac{(H_{k-1}+H_k)\,d^{(0)}_{k+\frac{1}{2}} + H_{k+1}d^{(0)}_{k-\frac{1}{2}}}{H_{k+1}+H_k+H_{k-1}} \\ \delta_k^L &= H_k\frac{H_{k-1}d^{(0)}_{k+\frac{1}{2}} + (H_k+H_{k+1})\,d^{(0)}_{k-\frac{1}{2}}}{H_{k+1}+H_k+H_{k-1}}\,, \end{aligned} \tag{4.72}$$

[7] In should be noted that in Colella & Woodward, 1984 if one substitutes expressions for δa_j and δa_{j+1} from (1.7) into (1.6) without subjecting them first to slope limiting (1.8), then both $2\Delta\xi_j + \Delta\xi_{j+1}$ and $\Delta\xi_j + 2\Delta\xi_{j+1}$ cancel out, and the final expression for $a_{j+\frac{1}{2}}$ is equivalent to one to described here.

Since $f(x)$ is a monotone function of its argument (which can be verified by showing that its first derivative is always positive), it reaches its extremal values at the minimum and maximum values of the argument, so is sufficient to show that

$$\frac{1}{2} \le \left| f\left(\frac{H_k}{\Delta_4}\right) \right| \qquad \text{and} \qquad \left| f\left(\frac{\Delta_4}{H_k}\right) \right| \le 2 \tag{4.80}$$

which can be verified by direct substitition of (4.76) and (4.79),

$$f\left(\frac{H_k}{H_{k-1}+2H_k+H_{k+1}}\right) = \frac{H_k+H_{k+1}}{2H_k+H_{k+1}} \ge \frac{1}{2} \tag{4.81}$$

and

$$f\left(\frac{H_{k-1}+2H_k+H_{k+1}}{H_k}\right) = \frac{H_{k-1}+2H_k}{H_{k-1}+H_k} \le 2\,. \tag{4.82}$$

This also proves that as long as H_k are positive, then $f(x)$ actually never reaches $\frac{1}{2}$ and 2, which means that parabolic segments inside each grid box cannot be saturated in sense that derivative at one end becomes zero, while distinct from zero at the other end.

$$\frac{2}{3} \le f(x) \le \frac{3}{2} \qquad \text{as long as} \qquad \frac{1}{4} \le x \le 4\,. \tag{4.83}$$

The consequence of this effect will be discussed later.

Profiles reconstructed by algoritm defined by (4.75)–(4.77), (4.70), (4.65) are shown in Fig. 9 . Despite the fact that all interfacial values fall within the bounds set by (4.71) and all interfacial derivatives have correct sign, oscillations of the interplant are present at coarse resolution and overall error is no significantly better than that of PPM with monotonicity constraint (4.58) turned off, but slope-limiting still in place, Fig. 7 , lower panel. Thought at fine resolution this algorithm will be shown to have better convergence rate than PPM and even parabolic spline, for the practical purposes it is not a good candidate to replace either one.

Computational cost: Computation of the initial settings of $\rho_{k+\frac{1}{2}}$ requires three divisions per each grid box to compute

$$\frac{1}{H_k+H_{k+1}}\,, \qquad \frac{1}{H_{k-1}+H_k+H_{k+1}}\,, \qquad \frac{1}{H_{k-1}+H_k+H_{k+1}+H_{k+2}}\,,$$

which are involved in coefficients for the polynomial interpolant. In addition to that, two more division are associated with the slope-limiting algorithm from Colella & Woodward, 1984,

$$\frac{1}{2H_k+H_{k+1}}\;; \qquad \frac{1}{H_k+2H_{k+1}}\,.$$

(Alternative slope-limiting algorithm (4.75)–(4.77) does not require these divisions.) These five divisions dominate the computational effort of PPM. The remaining cost is associated with the logical operations of monotonization procedure, which, however may be efficiently implemented through min/max functions.

4.5. Weighted ENO Family

Another potentially useful class of reconstruction algorithms which achieve high-order accuracy, while maintaining non-oscillatory behavior is the Essentially Non-Oscillatory (ENO) methods, Harten *et al*, 1987; Liu *et al*, 1994. The idea here is to compute interfacial value using several *candidate* stencils around the point, which will result in different values. The final version for the interfacial value is then obtained as a weighted sum of the candidate values, where weights depend on the *smoothness* of the interpolants obtained on the different stencils, in such a way that the smoothest stencil gets the maximum weight.

In this section we will show that this idea may be successfully adapted for reconstruction of density profiles after several modifications. Since ENO methods were originally designed for the advection problem, they sumply find the interfacial values. For our purposes we need not only a good estimate for the interfacial values, but also a well behaved interpolant, which is then integrated to get pressure distribution.

At first we compute ρ_k^R and ρ_k^L for all $k = 1, \ldots, N$ using steps (4.75)–(4.77), (4.58) and (4.70), after which at each grid-box interface $k+\frac{1}{2}$ we have two candidate values ρ_k^R and ρ_{k+1}^L, which are not necessarily equal to each other. Then, instead of using upper equation (4.65), which is, in effect, a weighted average of the two values, with weights being determined from the sizes of the respective grid boxes, we now set weights to be inversely proportional to a power of internal variation of the monotonized parabolic interpolant,

$$\rho_{k+\frac{1}{2}} = \frac{\rho_k^R/W_k + \rho_{k+1}^L/W_{k+1}}{1/W_k + 1/W_{k+1}} \tag{4.84}$$

where

$$W_k = \left|\rho_k^R - \rho_k^L\right|^n \equiv \left|\delta_k^R + \delta_k^L\right|^n \quad \forall\ k = 1, \ldots, N\,, \tag{4.85}$$

where n is a positive integer number. Choice of $n = 2$ in the case of smooth field (i.e., the first derivative does not change significantly from grid box to grid box) and a first derivative at the interface $k + \frac{1}{2}$,

$$\left.\frac{\partial\rho}{\partial z}\right|_k^R - \left.\frac{\partial\rho}{\partial z}\right|_{k+1}^L = \frac{4\rho_{k+\frac{1}{2}} + 2\rho_{k-\frac{1}{2}} - 6\overline{\rho}_k}{H_k} + \tag{4.87}$$
$$+\frac{4\rho_{k+\frac{1}{2}} + 2\rho_{k+\frac{3}{2}} - 6\overline{\rho}_{k+1}}{H_{k+1}}$$

To eliminate the mismatch, one can set $\rho_{k+\frac{1}{2}}$ to the special value,

$$\rho^*_{k+\frac{1}{2}} = \frac{(3\overline{\rho}_{k+1} - \rho_{k+\frac{3}{2}})H_k + (3\overline{\rho}_k - \rho_{k-\frac{1}{2}})H_{k+1}}{2(H_k + H_{k+1})}\,, \tag{4.88}$$

which, however does not solve the problem because once $\rho_{k+\frac{1}{2}}$ is replaced with $\rho^*_{k+\frac{1}{2}}$ for all k, $\rho_{k-\frac{1}{2}}$ and $\rho_{k+\frac{3}{2}}$ also become different from the original values, and the mismatch of derivatives (4.87) does not disappear entirely.

Instead, we consider an iterative procedure. Firsr we assign

$$\rho^{(0)}_{k+\frac{1}{2}} = \frac{\overline{\rho}_{k+1}H_k + \overline{\rho}_k H_{k+1}}{H_k + H_{k+1}}\,; \qquad k = 1, \dots, N-1\,, \tag{4.89}$$

then, for all $m = 0, 1, 2, \dots$,

$$\rho^{(m+1)}_{k+\frac{1}{2}} = \rho^{(m)}_{k+\frac{1}{2}} + \omega\left[\frac{3}{2}\rho^{(o)}_{k+\frac{1}{2}} - \rho^{(m)}_{k+\frac{1}{2}} - \frac{1}{2}\frac{\rho^{(m)}_{k+\frac{3}{2}}H_k + \rho^{(m)}_{k-\frac{1}{2}}H_{k+1}}{H_k + H_{k+1}}\right] \qquad k = 1, \dots, N-1\,, \tag{4.90}$$

where the term in square brackets can be viewed as the correction to $\rho^{(m)}_{k+\frac{1}{2}}$, while ω is the *underrelaxation* coefficient [if $\omega = 1$ (4.90) repeats (4.88)]. With the optimal choice of $\omega = {}^2\!/_3$ (Appendix D) the procedure (4.89)–(4.90) converges toward the parabolic spline values of $\rho_{k+\frac{1}{2}}$, and the convergence rate is very high: $\rho^{(1)}_{k+\frac{1}{2}}$ already recovers the fourth order of accuracy of spline-interpolated values. Procedure (4.89)–(4.90) requires two boundary conditions at top and bottom. These may be done by several different ways depending on the underlying physical boundary conditions in a manner similar that for parabolic spline. For example, Neumann b.c. imply that values $\rho^{(m+1)}_{N+\frac{1}{2}}$ and $\rho^{(m+1)}_{\frac{1}{2}}$ are set to

$$\rho^{(m+1)}_{N+\frac{1}{2}} = \frac{3}{2}\overline{\rho}_N - \frac{1}{2}\rho^{(m+1)}_{N-\frac{1}{2}} \tag{4.91}$$

$$\rho^{(m+1)}_{\frac{1}{2}} = \frac{3}{2}\overline{\rho}_1 - \frac{1}{2}\rho^{(m+1)}_{\frac{3}{2}} \tag{4.92}$$

every time after every iteration (4.90), so that $\rho^{(m+1)}_{N-\frac{1}{2}}$ and $\rho^{(m+1)}_{\frac{3}{2}}$ become available. (Eq. (4.91) stems from the assumption that density has parabolic distribution inside grid box H_N, such that its grid-box average is equal to $\overline{\rho}_N$, its value at the lower interface is equal to $\rho^{(m+1)}_{N-\frac{1}{2}}$, and its derivative at the upper interface vanishes. Eq. (4.92) is derived from a similar assumptions.) Alternatively, a linear extrapolation rule

$$\rho^{(m+1)}_{N+\frac{1}{2}} = 2\overline{\rho}_N - \rho^{(m+1)}_{N-\frac{1}{2}} \tag{4.93}$$

$$\rho^{(m+1)}_{\frac{1}{2}} = 2\overline{\rho}_1 - \rho^{(m+1)}_{\frac{3}{2}} \tag{4.94}$$

may be applied in a similar way. Profiles reconstructed by this procedure are shown in Fig. 11 where only two steps (4.90) were used (i.e., shown here is $\rho^{(2)}$). The result is, indeed, very similar to that on the upper panel of Fig. 4, with the difference between the two clearly smaller than the level of error relatively to the exact profile, which indicates that further continuation of the iterative procedure does not lead to any gain in accuracy. Similarly to parabolic spline, the reconciliation algorithm exhibits oscillations at coarse resolution.

To control the oscillations, we incorporate two measures into the procedure. First, each time after (4.90) is applied, we restrict the resultant interfacial values by bounds set by the adjacent grid-box values,

$$\begin{aligned}\rho^{(m'+1)}_{k+\frac{1}{2}} &= \min\left(\rho^{(m+1)}_{k+\frac{1}{2}}\,,\ \max\left(\overline{\rho}_k\,,\ \overline{\rho}_{k+1}\right)\right)\\ \rho^{(m''+1)}_{k+\frac{1}{2}} &= \max\left(\rho^{(m'+1)}_{k+\frac{1}{2}}\,,\ \min\left(\overline{\rho}_k\,,\ \overline{\rho}_{k+1}\right)\right)\,,\end{aligned} \tag{4.95}$$

after which $\rho^{(m''+1)}_{k+\frac{1}{2}}$ is accepted as the final value for $\rho^{(m+1)}_{k+\frac{1}{2}}$. Second, inside each grid box we apply the monotonicity constraining algorithm (4.58). Since this may destroy the continuity of reconstructed profile across the grid box interface (for each original value of $\rho^{(m+1)}_{k+\frac{1}{2}}$ (4.58) produces two values, ρ^R_k and ρ^L_{k+1} which are potentially not equal to each other), after completion of (4.58) in each grid box $k = 1, \dots, N$, the resultant values are reconciled using a WENO-like weighted sum,

$$\rho^{(m+1)}_{k+\frac{1}{2}} = \frac{W_k \cdot \rho^L_{k+1} + W_{k+1} \cdot \rho^R_k}{W_k + W_{k+1}}\,; \qquad k = 1, \dots N-1\,, \tag{4.96}$$

where

$$W_k = \left(\rho^R_k - \rho^L_k\right)^2\,; \quad k = 1, \dots, N \tag{4.97}$$

is the quadratic variation of the interpolant within the grid box.

Profiles reconstructed by this modified algorithm are shown on the lower panel of Fig. 11. Oscillations are eliminated at the expense of possible discontinuity of the derivative. The profiles are similar to ones obtained by iterated PPM; however computational cost of the present method is much smaller. As in Fig. 11 , only two iterations are used. The results are overall similar to WENO, see Fig. 10; with the exception that parabolic reconciliation tends leave smaller discontinuities in the first derivative in places where the slope cannot be reconciled using parabolic fit (compare profiles with N=6,9,10). This distinction is explained by the fact that in the case of large relative change of grid box variation, the interfacial value set by WENO is dominated by one of the candidate values, and parabolic segments inside each grid box never get saturated, see (4.81)—(4.82) and paragraph after it. Parabolic reconciliation, on the other hand, tend to saturate the parabolic segments until limiting takes effect.

4.7. Power-Law Reconciliation

In the case of reasonably smooth data WENO and Parabolic Slope Reconciliation produce accurate, oscillation free profiles, but they unavoidably give up continuity of the first derivative, if slope changes too rapidly. Quartic fit provides a greater potential in maintaining continuity of the first derivative (see Fig. 12), but unlike in the case of parabolic fits, where coefficients can be easily constrained to enforce monotonicity (4.58), no such procedure exists for quartic fits. Even thought, finding extrema of quartic polynomials involve solving cubic equation, which in principle can be done analytically, solving an inverse problem – imposing constraints on coefficients to make sure that all roots fall outside the desired interval – is too cumbersome to be practical.

We therefore chose an alternative path. Consider a function

$$\Phi(\xi) = \alpha\xi^{\beta+2} - \gamma\xi^2 \,, \qquad (4.98)$$

where coefficients α and γ gamma re chosen in such a way that

$$\Phi(1) = 1 \qquad \text{and} \qquad \int_0^1 \Phi(\xi)\mathrm{d}\xi = 0 \,, \qquad (4.99)$$

which leads to monoparametric family, Fig. 13 ,

$$\Phi_\beta(\xi) = \frac{3}{\beta}\left[\left(1+\frac{\beta}{3}\right)\xi^{\beta+2} - \xi^2\right] , \qquad (4.100)$$

where the singularity at $\beta = 0$ is removable,

$$\Phi_0(\xi) = \lim_{\beta\to 0} \Phi_\beta(\xi) = \xi^2\left(1 + 3\ln|\xi|\right) , \qquad (4.101)$$

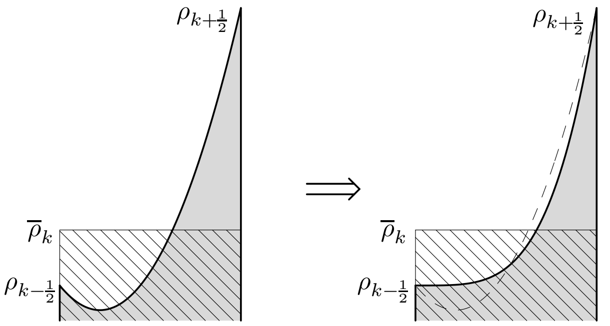

Figure 12. Monotone parabolic fit becomes impossible if $\overline{\rho}_k - \rho_{k-\frac{1}{2}}$ and $\rho_{k+\frac{1}{2}} - \overline{\rho}_k$ differ in magnitude by more than factor of 2, cf. Fig. 6 . Monotone quartic fit is still possible until this ratio is less than 4. Note that the shaded area is equal to the area of rectangle covered by diagonal lines.

and, obviously

$$\left.\frac{\partial\Phi_\beta}{\partial\xi}\right|_{\xi=0} = 0 \qquad \left.\frac{\partial^2\Phi_\beta}{\partial\xi^2}\right|_{\xi=0} = -\frac{6}{\beta} \qquad (4.102)$$

$$\left.\frac{\partial\Phi_\beta}{\partial\xi}\right|_{\xi=1} = \beta + 5 \,. \qquad (4.103)$$

Suppose a set of density distributions is computed within each grid box H_k by Parabolic WENO or Parabolic Slope Reconciliation, and there is discontinuity in first derivative at the interface $k+\frac{1}{2}$, ($d_k^R \neq d_{k+1}^L$, where d_k^R and d_{k+1}^L right and left side limits of derivatives of parabolic distributions in grid boxes H_k and H_{k+1} respectively, cf. (4.6)–(4.7) and (4.87).) which cannot be reconciled by a parabolic method without violation of parabolic monotonicity constraint (4.58), cf. Fig. 6 . Suppose we add

$$A\cdot\Phi_\beta\left(\frac{z'' + H_k}{H_k}\right) \qquad -H_k \le z'' \le 0 \qquad (4.104)$$

to the distribution $\rho(z'')$ within the grid box H_k (here and in (4.106) z'' is a local physical coordinate with origin at the interface $z_{k+\frac{1}{2}}$). This addition does not does not change the grid box average within H_k, value and derivative at the interface $k-\frac{1}{2}$, however at the interface $k+\frac{1}{2}$, the side limits of value and the first derivative are incremented by

$$A \qquad \text{and} \qquad \frac{A(\beta+5)}{H_k} \qquad (4.105)$$

respectively. Similarly, in the grid box H_{k+1} we add

$$A\cdot\Phi_\beta\left(\frac{H_{k+1} - z''}{H_{k+1}}\right) \qquad 0 \le z'' \le +H_{k+1} \,, \quad (4.106)$$

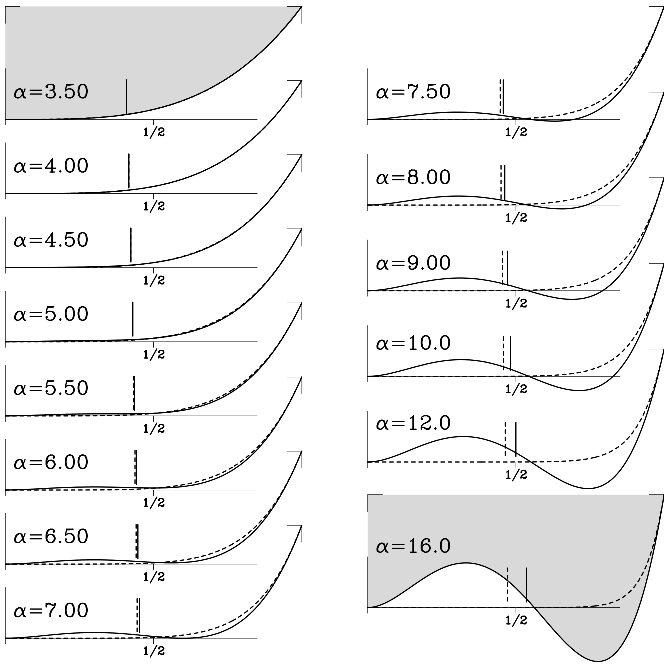

Figure 15. Comparison of ξ^α, $0 \le \xi \le 1$ (dashed curves) and its quartic polynomial fit (solid curves). The vertical dashed and solid lines indicate position of the center of gravity of area above the curves (shaded for $\alpha = 3.5$ and $\alpha = 16$).

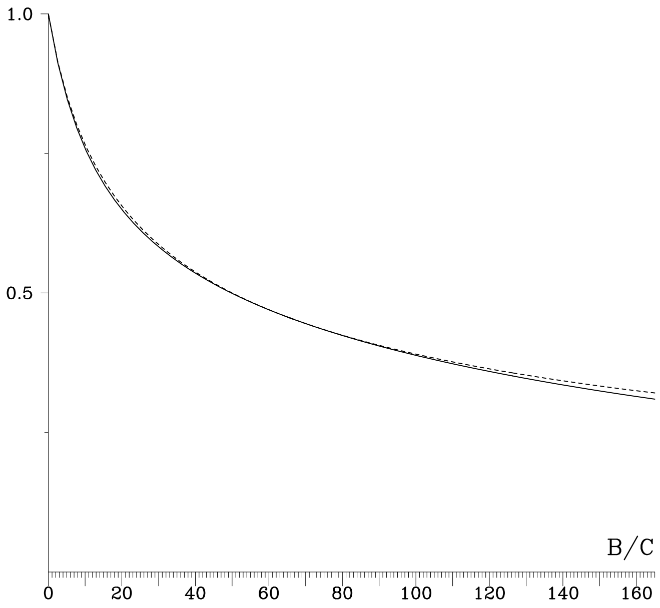

Figure 16. Comparison of limiting finction in r.h.s. of (4.122), dashed curve, with its rational function fit (4.124), solid curve, over the wide range of B/C ratios.

can verify that (4.112) and (4.115) are both autimatically satiffied as a consequence of (4.108)–(4.109).

Since interface $k+\frac{1}{2}$ is an irreconcilable point, distribution in one of the adjacent grid boxes is a saturated parabola, then the restriction (4.110)–(4.113) guaraneees that in the worst case scenario, if, for example, the distribution in the grid box H_k is saturated,

$$\rho(z'') = \rho_{k-\frac{1}{2}} + \left(\rho_{k+\frac{1}{2}} - \rho_{k-\frac{1}{2}}\right)\left(\frac{z''+H_k}{H_k}\right)^2 \quad (4.116)$$

and the sign of correction A (same as sign of $d^L_{k+1} - d^R_k$) is such that variation in the grid box H_k is to be increased, then the distribution (4.116) is replaced with

$$\rho(z'') = \rho_{k-\frac{1}{2}} + \left(A + \rho_{k+\frac{1}{2}} - \rho_{k-\frac{1}{2}}\right)\left(\frac{z''+H_k}{H_k}\right)^{\beta+2} \quad (4.117)$$

which is still monotonic.

After assignment

$$\begin{aligned} B &= \left(d'_{k+\frac{1}{2}} - d^R_k\right) H_k \\ C &= \left|\overline{\rho}_k - \rho_{k-\frac{1}{2}}\right| \end{aligned} \quad (4.118)$$

if the sign of $d^L_{k+1} - d^R_k$ mandates the use of (4.110)–(4.112), and $d'_{k+\frac{1}{2}}$ is the adjusted value of $d_{k+\frac{1}{2}}$, which satisfies (4.111), or

$$\begin{aligned} B &= \left(d^L_{k+1} - d'_{k+\frac{1}{2}}\right) H_{k+1} \\ C &= \left|\rho_{k+\frac{3}{2}} - \overline{\rho}_{k+1}\right| \end{aligned} \quad (4.119)$$

if (4.113)–(4.115) are to be used and $d'_{k+\frac{1}{2}}$ is adjusted to satisfy (4.114), Eqs. (4.110)–(4.115) may be rewritten as

$$A = \frac{B}{\beta+5} \quad \text{and} \quad \left|\frac{B}{\beta(\beta+5)}\right| \le C\,, \quad (4.120)$$

where we are interested in the minimum possible positive β, which is

$$\beta = \sqrt{\frac{25}{4} + \frac{|B|}{C}} - \frac{5}{2}\,, \quad (4.121)$$

which leads to

$$A = \frac{1}{5}B \cdot \frac{1}{\frac{1}{2} + \frac{1}{2}\sqrt{1 + \frac{4}{25}\cdot\frac{|B|}{C}}}\,, \quad (4.122)$$

the corrected interfacial value,

$$\rho'_{k+\frac{1}{2}} = \rho_{k+\frac{1}{2}} + A\,. \quad (4.123)$$

The effect of application of algorithm described here is illustrated on Fig. 14 .

Correction (4.122)–(4.123) should be compared with parabolic reconciliation (4.90). In fact, if $B \ll C$, so

Fig. 16 . Coefficients in (4.124) are set in such a way that its value and first derivative at B/C=0 and 66 concide with that of (4.122).

Fig. 17 shows series of profiles reconstructed by WENO enhanced by power-law reconciliation and distributions inside each grid box given by quartic fit. At this degree of non-smoothness, even if the interfacial values and derivatives would be exact, quartic fit exhibits mild oscillations, see Fig. 22 , therefore, it is fair to conclude that the proposed algorithm is well balanced on the coarse resolution end in sense that errors caused by inaccuracy of interfacial values are comparable with the accuracy of quartic fit itself and further improvement of accuracy of interfacial values does not lead to any reduction of eventual error in pressure gradient.

4.8. Preconditioned Quartic Spline

Since splines have the property of *global* dependency of interpolated values from the grid-box averaged values, prevention of oscillation requires *a priori* knowledge of places which cause the oscillations, rather than restriction of interfacial values after the spline is computed. This is because oscillations caused by sudden change in magnitude of the first derivative tend to penetrate into smooth regions dominating over the influence by local variation of grid-box values. Consequently, simple restriction, cf. (4.95), will just reset the interfacial values to one of the adjacent grid-box values, making it impossible to capture the correct structure of this part of the profile. Moreover, in this case even if the sequence of grid-box and interfacial values is monotone,

$$... \overline{\rho}_{k-1} \geq \rho_{k-\frac{1}{2}} \geq \overline{\rho}_k \geq \rho_{k+\frac{1}{2}} \geq \overline{\rho}_{k+1} ... \tag{4.125}$$

monotonicity of the reconstructed *continuous* profile is not guaranteed with violations similar to that in Fig. 7 .

Although accurate reconstruction of the details of smooth portions of the profile may seem to be not so crucial because the changes in values these are small in comparison with the changes which cause the oscillations, in the context of ocean modeling these smooth portions are typically associated with the abyssal part of the ocean, which lies below main thermocline, where vertical resolution is relatively coarse and motions are weak. As the result, relative errors associated with the "leak" of oscillations into abyssal regions may be too significant to ignore. Another problem stems from the fact that abyssal regions are typically weakly stratified, so that oscillations under these conditions may appear as regions of spurious negative stratification. This may have catastrophic consequences for the stability of the model even in the case when the set of discrete densities $\{\rho_k\,; \quad k=1,\,...\,N\}$ is monotone.

Suppose an approximation for the interfacial values $\rho_{k+\frac{1}{2}}$ and derivatives $d_{k+\frac{1}{2}}$ are computed by an algorithm with reliable coarse-resolution behavior, for example Weighted ENO or Parabolic Reconciliation algorithm. These values can be used to precondition spline algorithm. The idea of preconditioning is to replace some of the equations in the block-tri-diagonal system (4.32), similarly (4.28)–(4.31), with prescribed conditions,

$$\left.\begin{aligned} \rho_{k+\frac{1}{2}} &= \rho^{(0)}_{k+\frac{1}{2}} \\ d_{k+\frac{1}{2}} &= d^{(0)}_{k+\frac{1}{2}} \end{aligned}\right\} \quad k = k_1, k_2, ... \tag{4.126}$$

where $\rho^{(0)}_{k+\frac{1}{2}}$ and $d^{(0)}_{k+\frac{1}{2}}$ are the values determined by the preconditioning algorithm and $\{k=k_1,k_2,...\}$ is a subset of $\{k=1,\,...\,,N\}$ which is also determined by the preconditioning algorithm. Substitution of (4.32) by (4.126) means that the property of continuity of the second and third derivatives across some of the grid box interfaces [the design principle of (4.28)–(4.31)] is abandoned in favor of monotonicity constraints.

Eq. (4.126) also may be interpreted as a set of *internal* Dirichlet[9] boundary conditions for quartic spline algorithm effectively splitting the whole vertical column [the domain of dependency of the spline] into a set of closed intervals, which do not communicate with each other.

We generalize the idea of preconditioning by "softening" the preconditioner (4.126) with introduction of a predetermined function $\omega_{k+\frac{1}{2}}$ with possible values from the range $0 \leq \omega_{k+\frac{1}{2}} \leq 1$, which "blends" the the usage of Eqs. (4.126) vs. (4.32) in such a way that $\omega_{k+\frac{1}{2}}=0$ means that (4.32) is substituted by (4.126), while $\omega_{k+\frac{1}{2}}=1$ corresponds to the use of the original (4.32). Specifically we modify (4.41)–(4.42) so they become

$$\mathbf{C}_{k+\frac{1}{2}} = \omega_{k+\frac{1}{2}} \mathbf{B}'_{k+\frac{1}{2}} \cdot \mathbf{A}'_{k+1} \tag{4.127}$$

$$\begin{aligned} \mathbf{d}^*_{k+\frac{1}{2}} = \omega_{k+\frac{1}{2}} \mathbf{B}'_{k+\frac{1}{2}} \cdot \left(\mathbf{d}_{k+\frac{1}{2}} - \mathbf{A}_k \cdot \mathbf{d}^*_{k-\frac{1}{2}} \right) + \\ +(1-\omega_{k+\frac{1}{2}}) \mathbf{d}^{(0)}_{k+\frac{1}{2}} \end{aligned} \tag{4.128}$$

$$k = 1,2,\,...\,,N-1 \quad \text{in ascending order}$$

and $\mathbf{d}^{(0)}_{k+\frac{1}{2}}$ is symbolic vector notation for $\left(\rho^{(0)}_{k+\frac{1}{2}}\,,\, d^{(0)}_{k+\frac{1}{2}}\right)^T$.

[9] Dirichlet type in sense that the unknown function, which is in this case 2-vector $\left(\rho_{k+\frac{1}{2}}\,,\, d_{k+\frac{1}{2}}\right)^T$, is specified on the boundary.

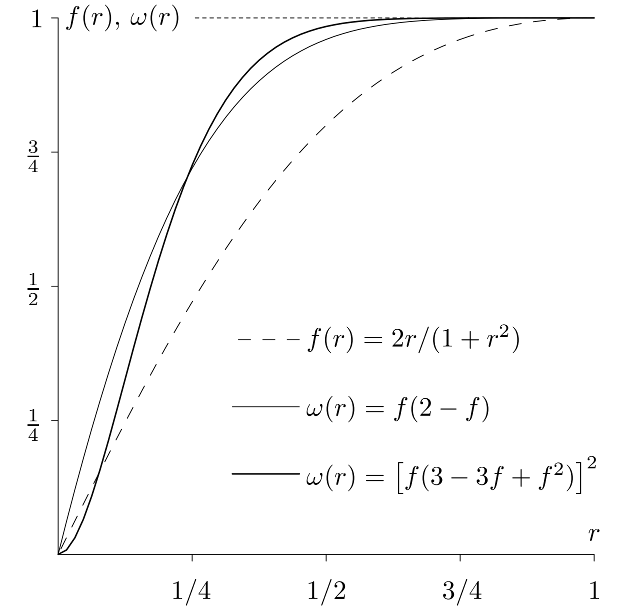

Figure 18. Weighting functions $f(r)$ and $\omega(r)$.

where $\rho_{\rm exact}$ is the exact profile and $h = \sum_{k=1}^{N} H_k$. In practice, integrals in (4.133) are evaluated by trapezoidal quadratic integration rule,

$$\int_{-H_k/2}^{+H_k/2} ... \approx \frac{H_k}{3M} \sum_{m=1}^{M} \left[(\mathcal{P}_m - \rho_m)^2 + (\mathcal{P}_m - \rho_m) \times \right. \qquad (4.134)$$
$$\left. \times (\mathcal{P}_{m-1} - \rho_{m-1}) + (\mathcal{P}_{m-1} - \rho_{m-1})^2\right] ,$$

on a uniform discretization of $M = 32$ intervals *within* each grid box. In (4.134) $\mathcal{P}_m, \rho_m = \mathcal{P}, \rho_{\rm exact}\left(H_k \frac{2m-M}{2M}\right)$, $m = 0, ... M$. Since both exact and reconstructed profiles are reasonably smooth functions within each grid box and M is sufficiently large, (4.133)–(4.134) provides an approximation of the continuous quadratically integrated measure with its own error due to discrete evaluation of integral (4.134). negligibly small.

There are two causes of reconstruction error:

(i) inaccuracy of the computation of interfacial values and/or derivatives; and

(ii) inaccuracy of parabolic or quartic hypothesis about the field structure inside the grid box.

Suppose the interfacial values and derivatives are known exactly. Then there is no contribution due to (i), but (ii) remains and is mostly due to the lowest order modes which are present in the exact solution, but cannot be captured by the parabolic and quartic polynomial fits,

$$\mathcal{P}^{(3)} = \xi\left(\xi^2 - \frac{1}{4}\right) ; \qquad \mathcal{P}^{(5)} = \xi\left(\xi^2 - \frac{1}{4}\right)^2 , \quad (4.135)$$

where the definition of local fractional coordinate ξ is the same as in (??)–(??) and, obviously,

$$\int_{-1/2}^{+1/2} \mathcal{P}^{(3,5)} {\rm d}\xi = 0 , \quad \mathcal{P}^{(3,5)}\Big|_{\xi=\pm\frac{1}{2}} = 0 , \quad \frac{\partial \mathcal{P}^{(5)}}{\partial \xi}\Big|_{\xi=\pm\frac{1}{2}} = 0 \quad (4.136)$$

which indicates that parabolic and quartic algorithms are insensitive to the addition of $\mathcal{P}^{(3)}$ and $\mathcal{P}^{(5)}$ modes. Since amplitudes of these modes are proportional to the third and fifth derivatives of the exact solution, the convergence rate of the parabolic and quartic fits in sense of measure (4.133) is expected to be N^{-3} and N^{-5} respectively. Comparison of polynomial fits based on exact and spline interfacial values is shown in Fig. 20 [10]. In the case of parabolic fits, the error is dominated by the error parabolic hypothesis [(ii)-type], which is manifested by the fact that the difference of errors of parabolic spline and parabolic fit based on exact interfacial values is small in comparison with the error measure of either one. For fine resolutions quartic spline behaves as an *asymptotically balanced* algorithm in sense that contributions of (i) and (ii)-types are comparable in magnitude and have the same rate of convergence: if taken separately, neither increase of order of accuracy of computation of interfacial values and derivatives, nor further increase of order of polynomial fit will result in increase of convergence rate. We refer this property as *quartic accuracy.* In contrast to that and to parabolic spline, for coarse resolutions error of quartic algorithm is dominated by the errors of computation of interfacial values and derivatives, [(ii)-type], while quartic fit based on exact interfacial values is extremely accurate in comparison with all other methods, even in the case of coarsest resolution, Fig. 22 .

In fact, none of the practical algorithms described in this section is able to fully utilize the capability of quartic fit to approximate transcendental functions. Moreover, quartic spline is the least robust method in computation of these interfacial values in the case of coarse resolution. This situation leads us to advocate the use of *pseudo*quartic methods, those which use quartic polynomial fit, but compute interfacial values using alternative

[10] All calculations presented here are performed with 16 Byte precision, which guarantees 31 decimal digit of accuracy. This competely excludes any possibility of influence of round-off errors onto analysis in Fig. 20 and Fig. 21 .

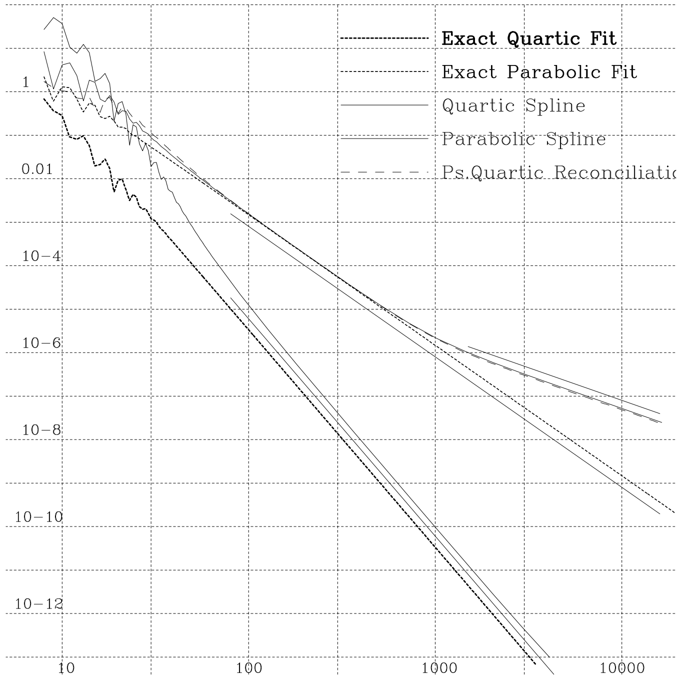

Figure 20. Comparison of convergence properties of parabilic and quartic polynomial fits based on *exact* and computed by splines interfacial values and derivatives. Horizontal axis: vertical resolution N of nonuniform grid; vertical axis: error measure. Straight lines correspond to convergence rates $N^{-3/2}$, N^{-3} and N^{-5}.

means, even if the resultant methods are not asymptotically balanced in terms of orders of accuracy as defined above.

Another conclusion from the fact that for the practically feasible range of resolutions (say $N = 20, \ldots, 50$) quartic algorithm errors are most likely to be dominated by the interfacial value errors, results shown in Fig. 20 [(ii)-type errors are about 10 ... 30 times larger than (i)-type] lead to the practical limit of "inconsistency" of the grid in sense of parameter r in (3.25), before substantial loss of accuracy occurs: The error of computation $FX_{i,j,k}$ term in (3.6) or (3.7) is likely dominated by the errors in computation of $\rho_{i,j,k+\frac{1}{2}}$ and $d_{i,j,k+\frac{1}{2}}$, [(i)-type] which in its turn tend to decrease with decrease of local vertical grid spacing $H_{i,j,k}$ with convergence rate $N^{-2}, \ldots, N^{-4}$, depending on particular method used (we do not expect them to decrease with full quartic rate in any practical application). The same values of $\rho_{i,j,k+\frac{1}{2}}$ and $d_{i,j,k+\frac{1}{2}}$ are used to compute $FC_{i+\frac{1}{2},j,k+\frac{1}{2}}$ according to (3.11) or (3.14). At the same time, errors of (ii)-type in computation of $FX_{i,j,k}$ and $FC_{i+\frac{1}{2},j,k+\frac{1}{2}}$ are expected to scale respectively as

$$H^n \quad \text{and} \quad \left(\Delta x \left.\frac{\partial z}{\partial x}\right|_{s=\text{const}} \right)^n , \qquad (4.137)$$

where $n = 3$ for parabolic and $n = 5$ for quartic algorithms [cf. (3.1)–(3.2)]. Refinement of vertical resolution alone $H \to 0$ does not lead to decrease of the term on the right in (4.137), so eventually the error of (ii)-type in computation of $FC_{i+\frac{1}{2},j,k+\frac{1}{2}}$ becomes comparable to that of (i)-type and then becomes dominant. This sets the practical limit of "grid inconsistency",

$$r = \frac{\Delta x}{H} \left.\frac{\partial z}{\partial x}\right|_{s=\text{const}} = \left[\frac{\text{Error } (i)\text{-type in } FX_{i,j,k}}{\text{Error } (ii)\text{-type in } FX_{i,j,k}} \right]^{1/n} \qquad (4.138)$$

beyond which any further vertical refinement does not lead to decrease of hydrostatic error of the pressure gradient scheme. According to Fig. 20 , for the profile used in our test problem, the term in square brackets can be estimated as of order of unity for the parabolic fits and order of 30 for quartic and pseudoquartic, which leads to the estimate

$$r \approx 1 \,, \qquad r \approx 30^{1/5} \approx 2 \qquad (4.139)$$

for parabolic and quartic fits respectively. This also indicates that quartic algorithms are more tolerant to steepness of topography which leads to inconsistent grids.

Convergence of practical algorithms described in this section are shown in Fig. 21 .

From point of view of error measure (4.133), asymptotic convergence rate of parabolic spline algorithm is $N^{-3/2}$ although the interfacial values are obtained with 4th order of accuracy. Post-smoothing of derivatives, see Eq. (C.29) in Appendix C, significantly reduces the error over large range of resolutions, but in fact, does not change the asymptotic order of accuracy of the scheme, not any decrease of error for the corsest resolutions. As expected, parabolic reconciliation (in its pseudo quartic version) algorithm produces results which are asymptotically similar to the parabolic spline, but is much more accurate in the case of coarse resolution because of its non-oscillatory properties. Weighted ENO has better asymptotic behavior than reconciliation algorithm, but it is less accurate over the whole range of coarse and intermediate resolutions. Quartic spline shows the fastest rate of convergence (N^{-5}) and the largest error at coarse resolutions at the same time, which is obviously attributed to oscillations.

Right panel in Fig. 21 shows the coarse resolution part of the left panel. This comparison reveals that for

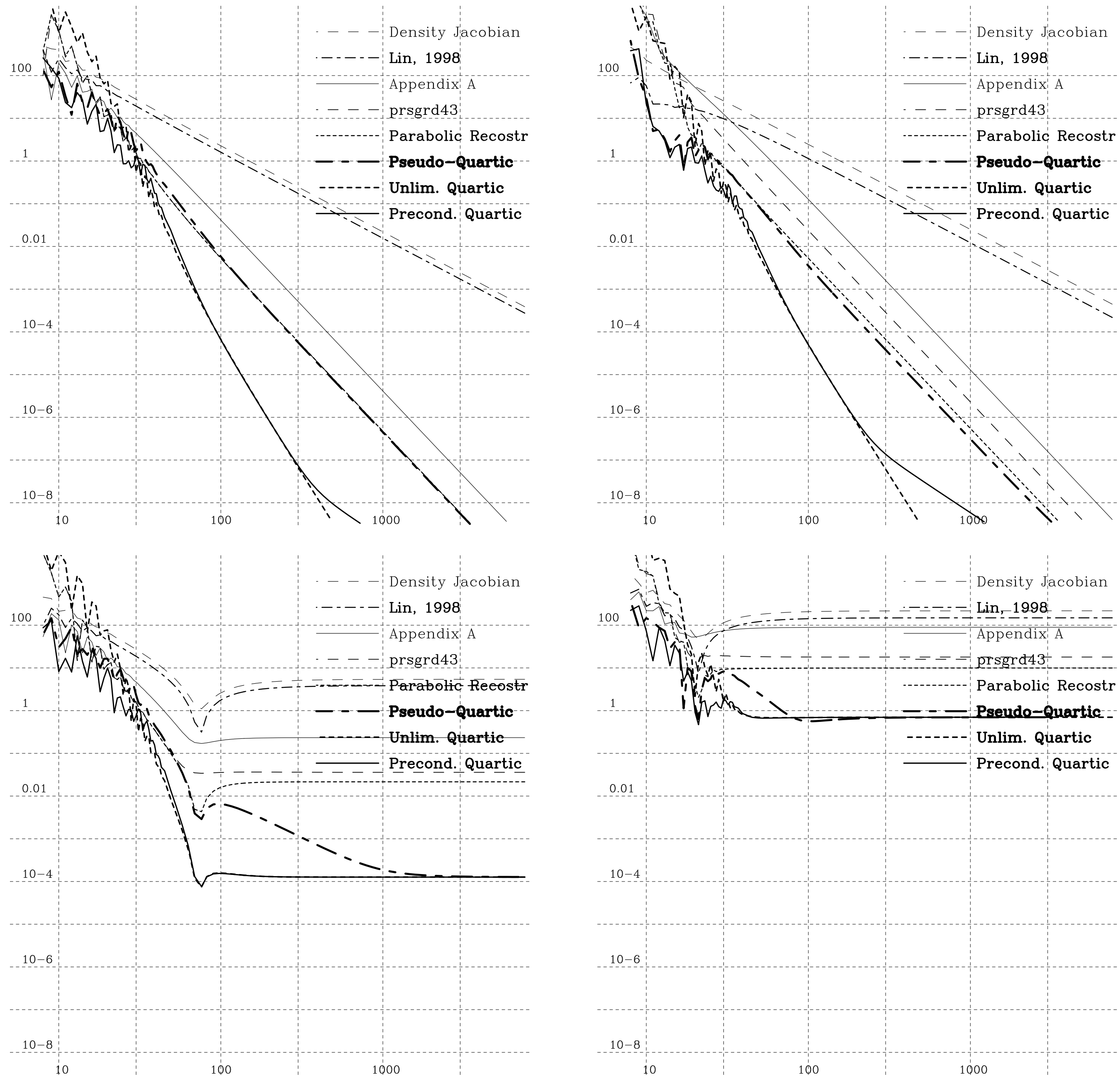

Figure 24. Asymptotic convergence of hydrostatic pressure gradient error. **Left side**: top – proportional refinement, bottom – refinement of vertical grid spacing only; **Right side**: the same as on the left, but topography slope is four times stronger. Note that labels for each curve are arranged top to bottom according to the rank of error for large resolution.

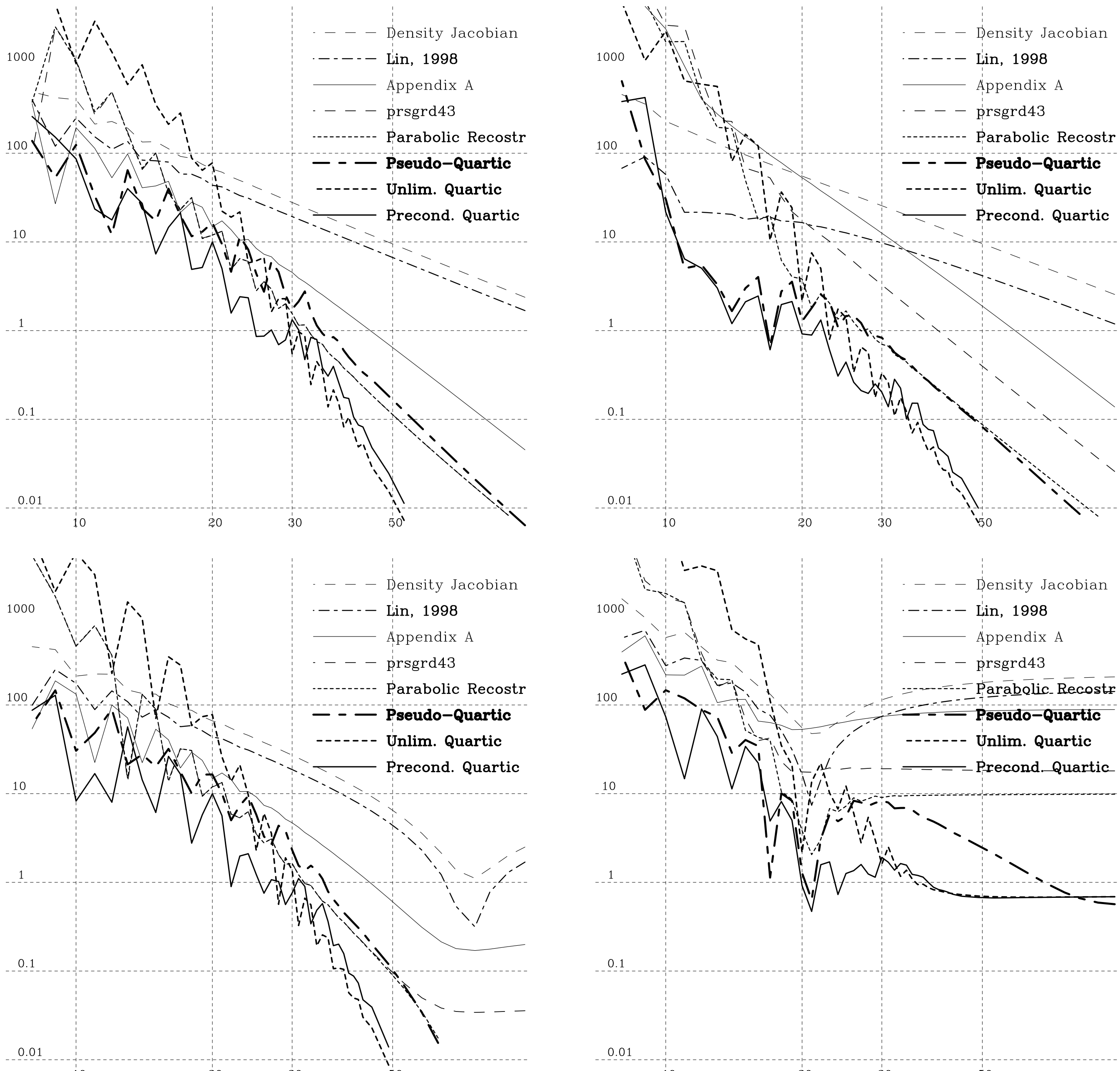

Figure 26. Enlarged coarse-resolution portion of Fig. 24 .

The idea here is to construct polynomial interpolants for both P and z as functions of s or ξ, which are then integrated analytically. As long as the interpolation algorithm is the same for both P and z, the resultant discrete Jacobian

$$J(P,z) = FX_{i,k} + FC_{i+\frac{1}{2},k+\frac{1}{2}} - \\ -FX_{i+1,k} - FC_{i+\frac{1}{2},k-\frac{1}{2}} \tag{A1.3}$$

retains its antisymmetry

$$J(P,z) = -J(z,P)\,, \tag{A1.4}$$

which can be verified by integrating by parts

$$\int\limits_{-\frac{1}{2}}^{+\frac{1}{2}} P\frac{\partial z}{\partial s}\mathrm{d}s = Pz\Bigg|_{s=-\frac{1}{2}}^{s=+\frac{1}{2}} - \int\limits_{-\frac{1}{2}}^{+\frac{1}{2}} z\frac{\partial P}{\partial s}\mathrm{d}s \tag{A1.5}$$

and noting that all terms outside the integral cancel out, when all four integrals are substituted into (A1.3).

In the case when linear interpolation is used, the resultant scheme is equivalent to Lin's.

Consider a cubic Lagrangian interpolant,

$$f(\xi) = f^{(0)} + f^{(1)}\xi + f^{(2)}\frac{\xi^2}{2} + f^{(3)}\frac{\xi^3}{6}\,, \tag{A1.6}$$

where

$$\begin{aligned} f^{(0)} &= \frac{9}{16}\left(f_{\frac{1}{2}} + f_{-\frac{1}{2}}\right) - \frac{1}{16}\left(f_{\frac{3}{2}} + f_{-\frac{3}{2}}\right) \\ f^{(1)} &= \frac{9}{8}\left(f_{\frac{1}{2}} - f_{-\frac{1}{2}}\right) - \frac{1}{24}\left(f_{\frac{3}{2}} - f_{-\frac{3}{2}}\right) \\ f^{(2)} &= \frac{1}{2}\left(f_{\frac{3}{2}} - f_{\frac{1}{2}} - f_{-\frac{1}{2}} + f_{-\frac{3}{2}}\right) \\ f^{(3)} &= f_{\frac{3}{2}} - 3f_{\frac{1}{2}} + 3f_{-\frac{1}{2}} - f_{-\frac{3}{2}}\,, \end{aligned} \tag{A1.7}$$

so that it can be verified that $f(\xi) = f_{\pm\frac{1}{2}}$ if $\xi = \pm\frac{1}{2}$ and $f(\xi) = f_{\pm\frac{3}{2}}$ if $\xi = \pm\frac{3}{2}$.

If P and z are both approximated by (A1.6)–(A1.7), then integrals (A1.1) and (A1.2) reduce to

$$\begin{aligned} \int\limits_{-\frac{1}{2}}^{+\frac{1}{2}} P\frac{\partial z}{\partial \xi}\mathrm{d}\xi &= \int\limits_{-\frac{1}{2}}^{+\frac{1}{2}} \Bigg[P^{(0)} + P^{(1)}\xi + P^{(2)}\frac{\xi^2}{2} + \\ &\quad +P^{(3)}\frac{\xi^3}{6}\Bigg]\cdot\left[z^{(1)} + z^{(2)}\xi + z^{(3)}\frac{\xi^2}{2}\right]\mathrm{d}\xi \quad \text{(A1.8)} \\ &= P^{(0)}z^{(1)} + \frac{1}{24}P^{(0)}z^{(3)} + \frac{1}{24}P^{(2)}z^{(1)} + \\ &\quad + \frac{1}{12}P^{(1)}z^{(2)} + \frac{1}{320}P^{(2)}z^{(3)} + \frac{1}{480}P^{(3)}z^{(2)}\,, \end{aligned}$$

which may be further simplified by noting that

$$\begin{aligned} P^{(0)} + \frac{1}{8}P^{(2)} &= \frac{1}{2}\left(P_{\frac{1}{2}} + P_{-\frac{1}{2}}\right) \\ z^{(1)} + \frac{1}{24}z^{(3)} &= z_{\frac{1}{2}} - z_{-\frac{1}{2}}\,, \end{aligned}$$

(cf. (A1.7)), therefore,

$$\int\limits_{-\frac{1}{2}}^{+\frac{1}{2}} P\frac{\partial z}{\partial \xi}\mathrm{d}\xi = \left(P^{(0)} + \frac{1}{8}P^{(2)}\right)\cdot\left(z^{(1)} + \frac{1}{24}z^{(3)}\right) - \tag{A1.9}$$
$$-\frac{1}{12}P^{(2)}\left(z^{(1)} + \frac{1}{40}z^{(3)}\right) + \frac{1}{12}\left(P^{(1)} + \frac{1}{40}P^{(3)}\right)z^{(2)}\,,$$

which after substitution of (A1.7) yields

$$\begin{aligned} FX_{i,k} &= \frac{1}{2}\left(P_{i,k+\frac{1}{2}} + P_{i,k-\frac{1}{2}}\right)\left(z_{i,k+\frac{1}{2}} - z_{i,k-\frac{1}{2}}\right) \\ &- \frac{1}{1440}\Bigg\{\left[P_{i,k+\frac{3}{2}} - P_{i,k+\frac{1}{2}} - P_{i,k-\frac{1}{2}} + P_{i,k-\frac{3}{2}}\right] \\ &\times\left[63\left(z_{i,k+\frac{1}{2}} - z_{i,k-\frac{1}{2}}\right) - \left(z_{i,k+\frac{3}{2}} - z_{i,k-\frac{3}{2}}\right)\right] \\ &- \left[63\left(P_{i,k+\frac{1}{2}} - P_{i,k-\frac{1}{2}}\right) - \left(P_{i,k+\frac{3}{2}} - P_{i,k-\frac{3}{2}}\right)\right] \\ &\times\left[z_{i,k+\frac{3}{2}} - z_{i,k+\frac{1}{2}} - z_{i,k-\frac{1}{2}} + z_{i,k-\frac{3}{2}}\right]\Bigg\} \end{aligned} \tag{A1.10}$$

and

$$\begin{aligned} FC_{i+\frac{1}{2},k+\frac{1}{2}} &= \frac{1}{2}\left(P_{i+1,k+\frac{1}{2}} + P_{i,k+\frac{1}{2}}\right)\times \\ &\times\left(z_{i+1,k+\frac{1}{2}} - z_{i,k+\frac{1}{2}}\right) \\ &- \frac{1}{1440}\Bigg\{\left[P_{i+2,k+\frac{1}{2}} - P_{i+1,k+\frac{1}{2}} - P_{i,k+\frac{1}{2}} + P_{i-1,k+\frac{1}{2}}\right] \\ &\times\left[63\left(z_{i+1,k+\frac{1}{2}} - z_{i,k+\frac{1}{2}}\right) - \left(z_{i+2,k+\frac{1}{2}} - z_{i-1,k+\frac{1}{2}}\right)\right] \\ &- \left[63\left(P_{i+1,k+\frac{1}{2}} - P_{i,k+\frac{1}{2}}\right) - \left(P_{i+2,k+\frac{1}{2}} - P_{i-1,k+\frac{1}{2}}\right)\right] \\ &\times\left[z_{i+2,k+\frac{1}{2}} - z_{i+1,k+\frac{1}{2}} - z_{i,k+\frac{1}{2}} + z_{i-1,k+\frac{1}{2}}\right]\Bigg\} \end{aligned} \tag{A1.11}$$

which, along with (A1.3) comprises an algorithm for computation of pressure gradient force.

Eq. (A1.10) cannot be applied at the grid boxes adjacent to the top ($k = N$) and bottom ($k = 1$), because it would require $P_{i,N+\frac{3}{2}}$ and $P_{i,-\frac{1}{2}}$, which are not available. The simplest way to address this problem is to use one-sided parabolic fit for P and z,

$$f(\xi) = \frac{3}{8}f_{\frac{1}{2}} + \frac{3}{4}f_{-\frac{1}{2}} - \frac{1}{8}f_{-\frac{3}{2}} + \left(f_{\frac{1}{2}} - f_{-\frac{1}{2}}\right)\xi \\ + \frac{1}{2}\left(f_{\frac{1}{2}} - 2f_{-\frac{1}{2}} + f_{-\frac{3}{2}}\right)\xi^2 \tag{A1.12}$$

as an alternative to (A1.6)–(A1.7), which results in

$$FX_{i,N} = \frac{1}{2}\left(P_{i,N+\frac{1}{2}} + P_{i,N-\frac{1}{2}}\right)\left(z_{i,N+\frac{1}{2}} - z_{i,N-\frac{1}{2}}\right)$$

where

$$\lambda = \lambda(\xi,\zeta) = \cos\xi + \cos\zeta - \cos(\xi+\zeta) - 1 \qquad \text{(B.10)}$$

and $\xi = \mathrm{k}_x\Delta x$, $\zeta = \mathrm{k}_z\Delta z$. Taylor expansion of $\lambda(\xi,\zeta)$ with respect to small ξ and ζ,

$$\lambda(\xi,\zeta) = \xi\zeta + \mathcal{O}\left(\xi^4,\, \xi^2\zeta^2,\, \zeta^4\right) \qquad \text{(B.11)}$$

which is consistent with the fact that the correction term $\Lambda[PX]$ is second-order small in comparison with PX in the same sense as error of second-order accuracy estimate of PX is smaller in comparison with the main term.

Since $\lambda(\xi,\zeta)$ reaches its maximum absolute value of 4 at $\xi = \zeta = \pm\pi$, then the restiction

$$|r| \leq 3 \qquad \text{(B.12)}$$

guarantees that the procedure (B.4) is stable. In the case of $r = 3$ operator $1 + \frac{r}{12}\Lambda$ is

$$1 + \frac{r}{12}\Lambda = \begin{bmatrix} -1/8 & +1/8 & \\ +1/8 & +3/4 & +1/8 \\ & +1/8 & -1/8 \end{bmatrix}. \qquad \text{(B.13)}$$

Appendix C: Fourier Analysis of Parabolic and Quartic Splines

On a uniform grid with spacing Δx Eq. (4.9) becomes[11],

$$\frac{1}{6}\rho_{j-\frac12} + \frac{2}{3}\rho_{j+\frac12} + \frac{1}{6}\rho_{j+\frac32} = \frac{\overline{\rho}_{j+1} + \overline{\rho}_j}{2}, \qquad \text{(C.1)}$$

while for the quartic spline algorithm, the analog of the system (4.28)–(4.31) is

$$\frac{4}{5}\frac{\rho_{j+\frac32} - \rho_{j-\frac12}}{2\Delta x} - \frac{d_{j-\frac12}}{20} + \frac{3}{10}d_{j+\frac12} - \frac{d_{j+\frac32}}{20} = = \frac{\overline{\rho}_{j+1} - \overline{\rho}_j}{\Delta x} \qquad \text{(C.2)}$$

$$\frac{7}{30}\rho_{j-\frac12} + \frac{8}{15}\rho_{j+\frac12} + \frac{7}{30}\rho_{j+\frac32} - -\frac{1}{30}\Delta x(d_{j+\frac32} - d_{j-\frac12}) = \frac{\overline{\rho}_{j+1} + \overline{\rho}_j}{2} \qquad \text{(C.3)}$$

For a Fourrier component

$$\rho(x) = \hat{\rho}_k \cdot e^{ikx}, \qquad \text{(C.4)}$$

[11] In the present part we adopt the following indexing convention: j is the spatial index on a uniform grid $x_j = \Delta x \cdot j$, k is used for Fourier component wavenumber, while i denotes imaginary unit. The correspondence of the present notation with that used in the rest of the article is established by the replacement rules $k \to j$, $H_k \to \Delta x$, where grid box height H_k looses its spatial index since the grid is becomes uniform.

the corresponding set of grid-box-averaged values is given by,

$$\overline{\rho}_j = \frac{1}{\Delta x}\int_{x_j-\frac{\Delta x}{2}}^{x_j+\frac{\Delta x}{2}} \hat{\rho}_k \cdot e^{ikx}\mathrm{d}x = \hat{\rho}_k \cdot \frac{\sin\left(\frac{\xi}{2}\right)}{\frac{\xi}{2}} e^{ik\Delta xj}, \qquad \text{(C.5)}$$

where we have introduced notation $\xi \equiv k\Delta x$. As a consequence of (C.5), the Fourier images of the r.h.ss of (C.1) and (C.2)–(C.3) are given by,

$$\frac{\overline{\rho}_{j+1} + \overline{\rho}_j}{2} = \hat{\rho}_k \cdot \frac{\sin(\xi/2)}{\xi/2}\cos\left(\frac{\xi}{2}\right) e^{ik\Delta x\left(j+\frac12\right)} \qquad \text{(C.6)}$$

$$\frac{\overline{\rho}_{j+1} - \overline{\rho}_j}{\Delta x} = ik\hat{\rho}_k \cdot \left(\frac{\sin(\xi/2)}{\xi/2}\right)^2 e^{ik\Delta x\left(j+\frac12\right)}, \qquad \text{(C.7)}$$

which leads to the Fourier analog of (C.1),

$$\left(\frac{2}{3} + \frac{1}{3}\cos\xi\right)\tilde{\rho}_k = \hat{\rho}_k\frac{\sin\xi}{\xi}, \qquad \text{(C.8)}$$

where $\tilde{\rho}_k$ is the Fourier amplitude of interfacial value, so that,

$$\rho_{j+\frac12} = \tilde{\rho}_k \cdot e^{ik\Delta x\left(j+\frac12\right)}. \qquad \text{(C.9)}$$

As a consequence of (C.8),

$$\tilde{\rho}_k = \hat{\rho}_k \cdot \frac{\frac{\sin\xi}{\xi}}{\frac23 + \frac13\cos\xi} \approx \hat{\rho}_k \cdot \left(1 - \frac{\xi^4}{180} + \dots\right). \qquad \text{(C.10)}$$

Ideally $\tilde{\rho}_k = \hat{\rho}_k$, so that the second term in curly brackets provides a measure of truncation error in terms of Taylor expansion for $\xi \to 0$. It formally establishes that the parabolic spline method has fourth order of accuracy for the interfacial values. Later we will demonstrate that its truncation error is significantly smaller than that of more conventional local cubic polynomial fit.

Similarly, spectral image of the system (C.2)–(C.3) is,

$$\frac{4}{5}\frac{i}{\Delta x}\tilde{\rho}_k\sin\xi + \left(\frac{3}{10} - \frac{1}{10}\cos\xi\right)\hat{d}_k = ik\hat{\rho}_k\frac{1-\cos\xi}{\xi^2/2} \qquad \text{(C.11)}$$

$$\left(\frac{8}{15} + \frac{7}{15}\cos\xi\right)\tilde{\rho}_k - \frac{i\Delta x}{15}\sin\xi \cdot \hat{d}_k = \hat{\rho}_k\frac{\sin\xi}{\xi} \qquad \text{(C.12)}$$

where $\hat{d}_k$ is the Fourier amplitude of interfacial derivative,

$$d_{j+\frac12} = \hat{d}_k \cdot e^{ik\Delta x\left(j+\frac12\right)}. \qquad \text{(C.13)}$$

First we note that (C.11)–(C.12) constitutes a well posed problem, since

$$\Delta = \begin{vmatrix} \frac45\frac{i}{\Delta x}\sin\xi & \frac15\left(\frac32 - \frac12\cos\xi\right) \\ \left(\frac{8}{15} + \frac{7}{15}\cos\xi\right) & -\frac{i\Delta x}{15}\sin\xi \end{vmatrix} = \qquad \text{(C.14)}$$

$$= -\frac{1}{300}\left[33 + 26\cos\xi + \cos(2\xi)\right] \neq 0$$

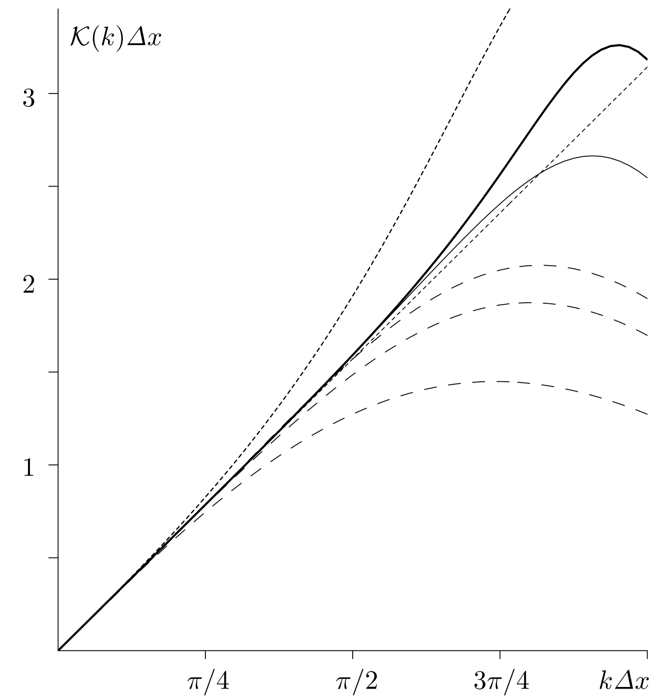

Figure 29. Spectral amplitudes of interfacial derivatives. Dashed curves from below up correspond to local polynomial fits from second- to sixth orders of accuracy. Bold dotted line (uppermost) — parabolic spline; Thin solid line — postsoothed parabolic spline derivatives; thick solid line — quartic spline.

Interfacial derivatives obtained by parabolic spline algorithm exhibit even stronger overestimate of Fourier amplitude at high wavenumbers. On a uniform grid these derivatives must satisfy the following tri-diagonal system,

$$\frac{1}{6}d_{j-\frac{1}{2}}+\frac{2}{3}d_{j+\frac{1}{2}}+\frac{1}{6}d_{j+\frac{3}{2}}=\frac{\overline{\rho}_{j+1}-\overline{\rho}_j}{\Delta x} \tag{C.25}$$

where $j=1,\dots,N-1$ and two boundary conditions are assumed at the sides. This results in Fourier amplitude for the interfacial derivative,

$$\hat{d}_k = ik\hat{\rho}_k\cdot\frac{1-\cos\xi}{\xi^2/2}\Big/\left(\frac{2}{3}+\frac{1}{3}\cos\xi\right)\approx \tag{C.26}$$
$$\approx ik\hat{\rho}_k\cdot\left(1+\frac{\xi^2}{12}+\dots\right),$$

indicating that the actual order of accuracy is only the second. In fact, the leading order truncation error is the same as for the simplest second-order differencing, with the exception that it has the opposite sign. The corresponding curve in Fig. 29 lies significantly above the ideal line. We will see soon that this effect is the major source of interpolation error for this algorithm and it can be corrected by an inexpensive procedure,

$$d'_{j+\frac{1}{2}}=\frac{5}{6}d_{j+\frac{1}{2}}+\frac{d_{j+\frac{3}{2}}+d_{j-\frac{1}{2}}}{12}. \tag{C.27}$$

In terms of Fourier amplitude, application of (C.27) is equivalent to multiplication of of (C.26) by $\frac{5}{6}+\frac{1}{6}\cos\xi$ which results in fourth order of accuracy for the derivative with the leading truncation term only twice as much in comparison with quartic spline algorithm,

$$\hat{d}'_k\approx ik\hat{\rho}_k\cdot\left(1+\frac{1}{15}\cdot\frac{\xi^4}{24}+\dots\right), \tag{C.28}$$

and it lies significantly closer to the ideal line in Fig. 29.

On a nonuniform grid the post-smoothing operator (C.27) becomes

$$d'_{k+\frac{1}{2}}=\frac{5}{6}d_{k+\frac{1}{2}}+\frac{1}{6}\cdot\frac{H_{k+1}d_{k-\frac{1}{2}}+H_k d_{k+\frac{3}{2}}}{H_k+H_{k+1}}, \tag{C.29}$$

which leads to inexpensive and accurate quartic *pseudo*-spline algorithm: obtain interfacial values $\rho_{k+\frac{1}{2}}$ and derivatives $d_{k+\frac{1}{2}}$ using usual parabolic spline algorithm, the apply (C.29) and use the sets of both $\rho_{k+\frac{1}{2}}$ and $d'_{k+\frac{1}{2}}$ in the same manner as it would be obtained by the quartic spline algorithm. This implies that the distributions within each grid box are given by fourth order polynomial.

Appendix D: Analysis of Convergence of Reconciliation Algorithm

The optimal choice of $\omega=2/3$ in the relaxation procedure (4.89)–(4.90) is explained as follows:

Consider a uniform grid, $x_j=\Delta x\cdot j$, then the analog of (4.89)–(4.90) is

$$\rho^{(0)}_{j+\frac{1}{2}}=\frac{\overline{\rho}_{j+1}+\overline{\rho}_j}{2} \tag{D.1}$$

$$\rho^{(m+1)}_{j+\frac{1}{2}}=\frac{3}{2}\omega\rho^{(o)}_{j+\frac{1}{2}}+(1-\omega)\rho^{(m)}_{j+\frac{1}{2}}-\omega\frac{\rho^{(m)}_{j+\frac{3}{2}}+\rho^{(m)}_{j-\frac{1}{2}}}{4} \tag{D.2}$$

For a Fourier component $\rho(x)=\hat{\rho}_k\cdot e^{ikx}$, the set of grid box values,

$$\overline{\rho}_j=\frac{1}{\Delta x}\int_{x_j+\frac{\Delta x}{2}}^{x_j+\frac{\Delta x}{2}}\rho(x')\mathrm{d}x'=\hat{\rho}_k\frac{\sin(\xi/2)}{\xi/2}\cdot e^{ik\Delta x\cdot j}, \tag{D.3}$$

where we have introduced $\xi\equiv k\Delta x$. Therefore,

$$\rho^{(0)}_{j+\frac{1}{2}}=\hat{\rho}_k\frac{\sin\xi}{\xi}\cdot e^{ik\Delta x\cdot(j+\frac{1}{2})}=\tilde{\rho}^{(0)}_k\cdot e^{ik\Delta x\cdot(j+\frac{1}{2})} \tag{D.4}$$

Janjic, Z. I., 1977: Pressure gradient force and advection scheme used for forecasting with steep and small scale topography. *Contrib. Atmos. Phys.*, **50**, 186–199.

Janjic, T., 1998: Comments on “A finite volume integration method for computing pressure gradient force in general vertical coordinates”, *Q. J. R. Meteorol. Soc.,*, **124**, 2527–2529.

Kliem, N., and J. D. Pietrzak, 1999: On the pressure gradient errors in sigma coordinate ocean models: A comparison with laboratory experiments. *Journ. Geophys. Res.*, **104**, 29,781-29,799.

Leer, van B., 1977: Towards the Ultimate Conservative Difference Scheme III. Upstream-centered Finite-Difference Schemes for Ideal Compressible Flow. *Journ. Comp. Phys.*, **23**, 263-275.

Lin, Shian-Jiann, 1997: A finite volume integration method for computing pressure gradient force in general vertical coordinates. *Q. J. R. Meteorol. Soc.,*, **123**, 1749-1762.

Lin, Shian-Jiann, 1998: Reply to comments by T. Janjic on “A finite volume integration method for computing pressure gradient force in general vertical coordinates”, *Q. J. R. Meteorol. Soc.,*, **124**, 2531–2533.

Liu, X.-D., S. Osher, and T. Chan, 1994: Weighted essentially non-oscillatory schemes, *Journ. Comp. Phys.*, **115**, 200-212.

Mahrer, Y., 1984: An improved numerical approximation of the horizontal pressure gradients in a terrain-following coordinate system. *Monthly Weather Review*, **112**, 918-922

McCalpin, J. D., 1994: A comparison of second-order and fourth-order pressure gradient algorithms in a σ-coordinate ocean model. *Int. J. of Num. Meth. in Fluids*, **18** , 361-383.

Mellor, G. L., T. Ezer and L.-Y. Oey, 1994: The pressure gradient conundrum of sigma coordinate ocean models. *Journ. Atmos. Oceanic Technology*, **1994**, 1126-1134.

Mellor, G. L., L.-Y. Oey, and T. Ezer, 1998: Sigma coordinate pressure gradient errors and the seamount problem. *Journ. Atmos. Oceanic Technology*, **15**, 1122-1131.

Mesinger, F., and A. Arakawa, 1976: Numerical Methods used in atmospheric models, Vol. 1, GARP Publ. Ser. 17., World Meteor. Org., 64 pp.

Mesinger, F., 1982: On the convergence and error problems of the calculation of the pressure gradient force in sigma coordinate ocean models. *Geophys. Astrophys. Fluid Dyn.*, **19**, 105-117.

Mesinger, F. and Z. I. Janjic, 1985: Problems and numerical methods of the incorporation of mountains in atmospheric models. *Lect. Appl. Math.*, **22**, 81-120.

Michailovic, D. T., and Z. I. Janjic, 1986: Comparison of methods for reducing the error of the pressure gradient force in sigma-coordinate models. *Meteorol. Atmos. Phys.*, **35**, 177-184.

Millero, F. J., C.-T. Chen, A. Bradshaw, and K. Schleicher, 1980: A new high-pressure equation of state for seawater. *Deep-Sea Res.*, **27A**, 255-264.

Shchepetkin, A. F. and J. J. O'Brien, 1996: A Physically Consistent Formulation of Lateral Friction in Shallow Water Equation Ocean Models. *Monthly Weather Review*, **124**, 1285-1298.

Slordal, L. H., 1997: The pressure gradient force in sigma coordinate ocean models. *Int. J. of Num. Meth. in Fluids*, **24** , 987-1017.

Song, Y. T. and D. Haidvogel, 1994: A Semi-implicit ocean circullation model using a generalized topography following coordinate system, *Journ. Comp. Phys.*, **115**, 228-248.

Song, Y. T. 1998: A General Pressure Gradient Formulation for Ocean Models. Part I: Scheme Design and Diagnostic Analysis, *Monthly Weather Review*, **126**, 3213-3230

Song, Y. T. and D. G. Wright, 1998: A General Pressure Gradient Formulation for Ocean Models. Part II: Energy, Momentum and Bottom Torque Consistency, *Monthly Weather Review*, **126**, 3213-3230

Stelling, G. S., and J. A. Th. van Kester, 1994: On the approximation of horizontal gradients in sigma coordinates for bathymetry with steep bottom slopes. *Int. J. of Num. Meth. in Fluids*, **18** , 915-935.

Treguier, A. M., J. K. Dukowicz, and K. Bryan, 1996: Properties of nonuniform grids used in ocean general circullation ocean models. *Journ. Geophys. Res.*, **101**, 20877-20881.